Factors Influencing the Signal Sensitivity in Searches for $Z' \to \tau_{had}\tau_{had}$ at $\sqrt{s} = 8$ TeV with the ATLAS Detector

Name: Catherine Hsu (359985)

Supervisor: Dr Oana Boeriu

August 11, 2014

A Dissertation Presented to

The Faculty of Science

University of the Witwatersrand

Johannesburg

In Fulfillment

of the Requirements of the Degree

Master of Science

Declaration

For this dissertation, I received assistance from Dr Katharine Leney on the programming side of the project. No parts of this dissertation have been submitted or are being submitted for qualification at another University.

Signed:

Abstract

The Z' gauge boson is a hypothetical neutral particle of spin-1 appearing in many theories beyond the Standard Model. In the context of the Z' boson of the Sequential Standard Model in the hadronic decay channel $Z' \to \tau_{had}\tau_{had}$, this project investigates improving the sensitivity of the analysis. It is important in the analysis to have high signal efficiency and to be able to distinguish against background processes, thus this project begins with an investigation into new triggers and their combinations that aim to improve the signal efficiency, followed by a study to improve the tau identification using tracking. The multi-jet background is focused on in the project because it is the dominant source of fake tau signatures in the detector. The data sample used was recorded by the ATLAS detector during the 2012 run of the Large Hadron Collider at a centre-of-mass energy $\sqrt{s} = 8$ TeV with an integrated luminosity of 19.5 fb^{-1}. Monte Carlo samples were compared with the data sample for various cut-based variables to investigate which of the variables offer a good discrimination power against the multijet background. The significance of each trigger and trigger combinations are shown, as well as the performance of different techniques and ideas used to improve the tau identification using tracking.

Since it is important in this project to be able to reconstruct a tau lepton from its hadronic decay products, this dissertation takes the opportunity to present preliminary results on the study of the light collection uniformity and response in the crack scintillation counters of the ATLAS hadronic tile calorimeter as part of the contribution towards the detector upgrade.

Acknowledgements

High energy physics has been fascinating for me for a long time, and after speaking to Professor Robert de Mello Koch, to whom I'm very grateful, introduced me to Dr Oana Boeriu. Since then Oana has been my supervisor, and I would like to thank her. Throughout the entire period, Oana has given me her never-ending help, support and encouragement. There was never a time that Oana was not patient and caring towards all the questions and problems I had, even if they were not related to the work on the project.

I would also like to thank Dr Katharine Leney for helping me continuously throughout the project. I could ask her any questions, present any problems and Katharine would help me and explain to me with great understanding and patience. Even with her busy schedule, Katharine was always there to lend a helping hand.

Last year I participated in the CERN Summer Student Programme, and I would like to thank my supervisor, Dr Trevor Vickey and Professor Bruce Mellado because without them I would not have had the opportunity to experience the excitement of being at CERN. I am also grateful towards CERN SA-ATLAS for providing me with funding.

Finally, I would like to thank my family for all their love and wisdom and support.

Contents

List of Figures

List of Tables

Chapter 1

Introduction

The European Organisation for Nuclear Research (CERN) is performing experiments using powerful accelerators to move forward our understanding of the Universe. At the Large Hadron Collider (LHC) at CERN proton beams are accelerated towards each other at the nearly the speed of light and collided at four experiments. Two are general purpose detectors: the ATLAS (A Toroidal LHC ApparatuS) [1] and CMS (Compact Muon Solenoid) [2] experiments, and two are specific detectors. One of them is ALICE (A Large Ion Collider Experiment) [3] which detects quark-gluon plasma, and the other is LHCb (Large Hadron Collider beauty) [4] which investigates the matter and anti-matter imbalance by studying the "beauty quark", or b-quark. These collisions cause many particles to be created, mostly those that are known and possibly those that are not. With every new discovery of particles or processes, our understanding of matter, energy, and symmetry breaking will change.

Z' bosons Beyond the Standard Model (BSM)

The Standard Model (SM) is the modern theory which emerged in the early 1970s and which describes the known fundamental particles and their interactions, except for gravity which is very weak at the atomic level. Even though the SM comprises a wide range of physics and has proven to be successful in explaining many experimental results, it does not, for example, include gravity, or explain the predominance of matter over anti-matter in the Universe. The SM also has 19 free parameters that need to be determined empirically [5]. As a result, theories beyond the SM (BSM) have been constructed in order to account for these observations. These theories expand on the gauge structure of the SM, and these extensions predict the existence of new particles. The hypothetical Z' boson is a massive and electrically neutral particle of spin-1 in some of the BSM theories [6]. At the LHC, Z' bosons are created from the annihilation of a quark with an anti-quark, and can decay into dileptons such as ditau (tau τ^- and an anti-tau τ^+), dimuon (muon μ^- and an anti-muon μ^+), or dielectron (electron e^- and a positron e^+) final states. The decay of a Z' boson also

includes a $\nu\bar{\nu}$ (neutrino and an anti-neutrino) pair, or a $q\bar{q}$ (quark and an anti-quark) pair. Its existence is an important one because it may shed light on why dark matter dominates the Universe, it could provide a stepping stone to the unification of the four fundamental forces of the Standard Model, and it could contribute to the search for extra dimensions [7].

Tau Leptons and Interests in them

Tau leptons are massive particles with a mass of 1.777 GeV and a proper decay length of 87 μm [6]. They are investigated because they play a significant role in the search for new physics [8]. Not only can the spin of the tau be used to separate signal from background, it can also be used to measure properties of new particles decaying into tau leptons, such as their polarisation, spin correlations, and their parity [9]. Many BSM theories with extended weak or hypercharge gauge groups, which account for the large mass of the top quark, postulate that heavy gauge bosons couple preferentially to third generation fermions, such as the tau leptons [10].

For this project, the reconstruction of the hadronic taus from the heavy neutral Z' gauge boson in the Sequential Standard Model (SSM) is studied. Tau leptons decay leptonically 35% of the time, or hadronically 65% of the time [6].

In the detector, quarks are reconstructed as a jet of hadrons thus it is difficult to differentiate between hadronic tau decays and gluon- or quark-initiated jets (QCD jets) [11]. This dissertation also investigated the performance of the scintillation counters of the ATLAS Tile Calorimeter because a good energy resolution of objects in the detector, and thus accurate particle identification, relies on the light uniformity in the scintillation counters. Another impact on the sensitivity of the analysis is that the decay products of a high transverse momentum (p_T) hadronically decaying object in dense environment may be detected as a single track in the detector, as opposed to a number of distinct tracks [12]. These collimated hadronic jets result in the track merging problem, and there have been studies [12, 13] that investigated algorithms which aimed at reducing the sensitivity of the jets to dense environments, or which could identify those decays that suffered the track merging. The studies showed promise, but the research is still ongoing.

For this project, various cut-based variables were investigated that attempt to resolve the tracks as well as to contribute to the discrimination between the multijet background and the signal of interest.

This dissertation begins with the theory of the SM and BSM theories in Chapter 2. Chapter 3 gives a description of the LHC and the ATLAS detector, and Chapter 4 presents the study of the scintillation counters of the ATLAS Tile Calorimeter. Chapter 5 describes

the data and Monte Carlo samples used for the trigger efficiency study and the study of tau identification using tracking. Both of these studies are presented in Chapter 5 as well. Chapter 6 summarizes the results.

Chapter 2

Theory

2.1 The Standard Model

In the SM [5], the fundamental particles and their interactions are described. There are three classes of fundamental particles: leptons, quarks and bosons. The matter particles, leptons and quarks, are fermions and are thus spin $\frac{1}{2}$ particles. Bosons are integer-spin particles. In each group of leptons and quarks there are six particles that are divided into doublets which form a so-called *generation*. There are three generations, and Figure 2.1 depicts this. The first generation is comprised of the lightest and most stable particles, and they compose all known matter in the Universe. The second and third generations contain the heavier and less stable particles. They thus decay with short half-lives to become more stable. Since these particles are heavier, higher energies are required for them to be studied. The SM also gives a description for the four fundamental forces in nature: the strong force, weak force, electromagnetic force and the gravitational force. The SM excludes gravity as its effects on a minute scale are negligible. The three fundamental interactions are the result of the mediation by bosons between matter particles.

The SM has the symmetry group $SU(3)_C \otimes SU(2)_L \otimes U(1)_Y$, where $SU(3)_C$ is the colour SU(3) symmetry, $SU(2)_L$ indicates that the SU(2) gauge transformations operate only on left-handed particles, and Y on U(1) stands for the hypercharge and it is used to indicate that it is different from the $U(1)$ for electromagnetism [**?**, 15]. The group $SU(3)$ describes the strong interactions which interact via 8 massless gauge bosons, the gluons. The $SU(2)$ group describes the weak interaction with three massless gauge bosons, and $U(1)$ refers to electromagnetism with its single massless gauge boson, the photon. $SU(2)_L \otimes U(1)_Y$ forms the electroweak theory which describes that at high energies, the electromagnetic force and the weak force unify into a single theory, and at low energies they are separate forces. The weak nuclear force is short range because the gauge bosons are very heavy. The method of spontaneous electroweak symmetry breaking was then constructed by theorists to make the

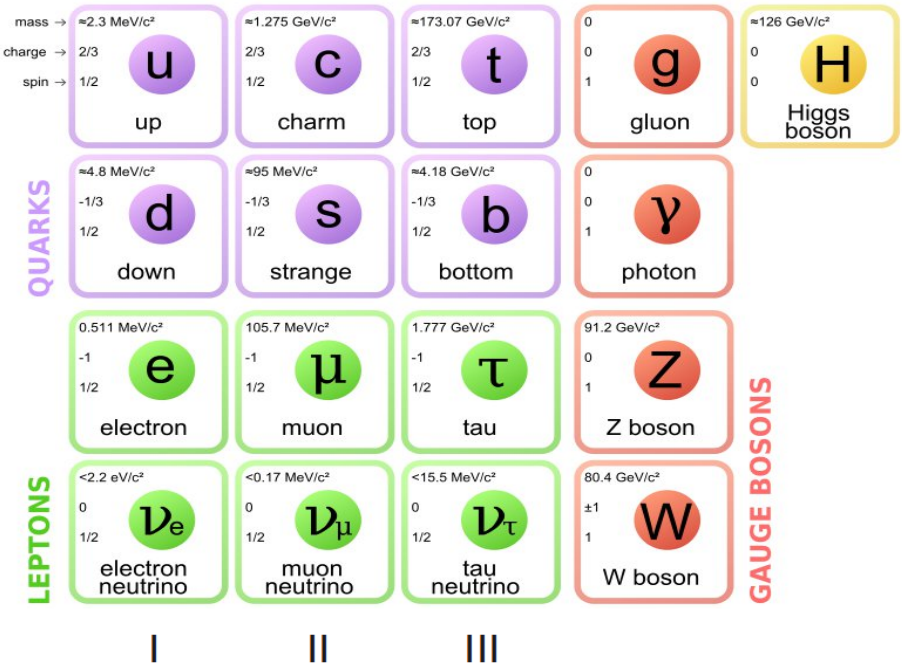

Figure 2.1: The SM is composed of three generations of particles which are divided into doublets [14].

gauge bosons massive while still preserving the renormalisation scheme of the gauge theory. In electroweak symmetry breaking a Higgs boson is produced, and the massless gauge bosons interact with the scalar Higgs field to acquire mass and thus become three massive gauge bosons: W^+, W^- and Z^0, as well as one massless gauge boson, the photon.

A discussion of the fundamental forces and particles will be given first. The material used for this has been extracted from Reference [15]. Afterwards, there is a look into the electroweak symmetry breaking of the SM Higgs sector.

2.1.1 The Four Forces

Strong Force

The strong force is a short range force that holds the quarks together to form the nucleons (protons and neutrons). The attractive force between nucleons arise from the strong interaction. Since protons and neutrons are composed of quarks, and quarks are bound together by the colour force, the strong force experienced by the nucleons may be considered as a "spill-over" of the colour force. Eight massless gluons are the exchange particles which mediate the strong interaction between quarks.

Weak Force

The weak interaction was discovered in decays involving β particles. Decays of nuclear particles are only possible if there is a flavour change from one quark to another, and the weak interaction is the only process that allows for this transmutation of quarks and leptons. The weak force is mediated by the exchange of the massive intermediate vector bosons, the $W^{\pm}$ and Z^0 boson. Leptons, quarks and neutrinos all participate in the weak interactions.

Electromagnetic Force

The electromagnetic (EM) force is apparent through the Coulomb interaction between electric charges and the magnetic force. The exchange of photons mediates the EM force since both the electric force and the magnetic force are the result of an exchange force involving photons. The EM force has an infinite range, and it determines the structures of atoms and molecules because the Coulomb interaction is so strong that it diminishes the effects of the other fundamental forces to influence the atomic and molecular structures.

Gravitational Force

Gravity is the weakest force but it is the most dominant at large scales. Gravitons are hypothesized to be the exchange particles that mediate the gravitational force, but these particles have not yet been observed.

2.1.2 The Fundamental Particles

Leptons

There are six leptons in the present structure which are arranged in pairs into three generations. They are classified according to their charge (Q), electron number (L_e), muon number (L_μ) and tau number (L_τ). The first generation is comprised of the electron (e) and the electron neutrino (ν_e), the second generation of the muon (μ) and the muon neutrino (ν_μ), and the third generation of the tau (τ) and the tau neutrino (ν_τ), as shown in Table 2.1. There exist, as well, six anti-leptons which have the same spin and mass as their corresponding particles, but with opposite charges. Leptons interact through the weak force, and the electromagnetic force if they are charged. Leptons do not carry colour charge and are thus not subjected to the strong force.

Table 2.1: Lepton Classification.

l	Generation	Q	L_e	L_μ	L_τ
e	1	-1	1	0	0
ν_e	1	0	1	0	0
μ	2	-1	0	1	0
ν_μ	2	0	0	1	0
τ	3	-1	0	0	1
ν_τ	3	0	0	0	1

Quarks

Like the leptons, there are also six types or flavours of quarks that are paired and divided into three generations, as shown in Table 2.2. The first generation contains the up (u) and the down (d) quark, while the second generation consists of the charm (c) and the strange (s) quark, and the third generation of the bottom (b) and the top (t) quark. The six flavours of quarks are arranged according to their charge (Q), and the quantum numbers: strangeness (S), charm (C), bottom (B), and top (T).

Table 2.2: Quark Classification.

q	Generation	Q	S	C	B	T
d	1	$-\frac{1}{3}$	0	0	0	0
u	1	$\frac{2}{3}$	0	0	0	0
s	2	$-\frac{1}{3}$	-1	0	0	0
c	2	$\frac{2}{3}$	0	1	0	0
b	3	$-\frac{1}{3}$	0	0	-1	0
t	3	$\frac{2}{3}$	0	0	0	1

Baryons are particles made up of three quarks. The most familiar baryons are the protons and the neutrons. Mesons are particles made up of two quarks. Since quarks are Dirac fermions, they have to obey the Pauli exclusion principle, which they do because each quark carries one of the three colour charges: red, blue and green. Due to colour confinement, quarks can never occur in isolation but only in bound states. Associated with each flavour of quark is their anti-quark. Quarks interact via the weak force, strong force, and the electromagnetic force.

Gluons

Gluons are the exchange particles for the colour force between quarks. They carry colour charge, thus, like the quarks, gluons do not exist as isolated particles. Gluons can also interact with each other which results in the strong force being limited in range.

Intermediate Vector Bosons

The W^+, W^-, and the Z^0 are massive exchange particles that mediate the weak interaction between leptons and between quarks. There are two types of weak interactions: the charged interaction which is mediated by the W gauge bosons, and the neutral interaction mediated by the Z bosons. The charged W bosons play a role in the transformation of one flavour of quark to another.

Photon

The photon is the exchange particle responsible for the electromagnetic force. It has a zero rest mass which results in the EM force being infinite in range. The photon can exert a force due to it having finite momentum, and being deflected by a gravitational field.

The Higgs Boson

The Higgs Boson is a spin-0 particle predicted in the SM to be a mediator of the action of the Higgs field. The Higgs field is a result of the Brout-Englert-Higgs (BEH) mechanism, and it was shown by the physicists Robert Brout, François Englert and Peter Higgs, in two separate papers, that this field must exist in order for the SM leptons and quarks to be mathematically consistent. The existence of the Higgs boson can verify the BEH mechanism and confirm the way in which particles gain mass [16].

In the SM, mass of the Higgs boson is given as

$$m_{hSM}^2 = \frac{1}{2}\lambda\nu^2 \tag{2.1}$$

where λ is the Higgs self-coupling parameter and ν is the vacuum expectation value (vev) of the Higgs field. Since this parameter is unknown, the SM cannot predict the Higgs boson's mass. Thus, one of the main reasons for the construction of the LHC at CERN was to search for the Higgs boson.

A ground-breaking event took place on July 4th 2012 that a particle consistent with the Higgs boson was discovered at CERN by the ATLAS and CMS experiments. The newly discovered particle was found to have a mass between 125-126 GeV, and it showed the characteristics of a SM Higgs bosons [17, 18].

2.1.3 Standard Model Higgs Sector

Spontaneous symmetry breaking occurs when the true symmetry of the system is hidden by a choice of vacuum, which is the ground state or the state of lowest potential energy. This mechanism generates the mass spectrum of the SM particles by introducing the Higgs field. Through spontaneous symmetry breaking, the Higgs field couples to the weak field to generate the masses of W and Z gauge bosons, as well as the mass of the other particles in the other SM sectors. This is the BEH mechanism, and in addition to it generating the mass spectrum of particles, it also produces the Higgs boson. Thus, proving the existence of the Higgs particle can confirm the BEH mechanism, and the manner in which particles gain mass.

The breaking of local U(1) gauge symmetry gives rise to the BEH mechanism. Eqn. 2.2 and Eqn. 2.3 defines, respectively, the scalar field and the Lagrangian:

$$\phi^*\phi = \phi_1^2 + \phi_2^2. \tag{2.2}$$

$$\mathcal{L} = \frac{1}{2}(\partial_\mu\phi)^*(\partial^\mu\phi) + \frac{1}{2}\mu^2(\phi^*\phi) - \frac{1}{4}\lambda^2(\phi^*\phi)^2 \tag{2.3}$$

The Lagrangian can be constructed to be invariant under local U(1) gauge transformation

$$\phi \rightarrow \phi' = e^{i\theta(x)}\phi \tag{2.4}$$

by the addition a massless gauge field A_μ, and replacing the partial derivative in Eqn. 2.3 with the covariant derivative

$$\mathcal{D} = \partial_\mu + iqA_\mu \tag{2.5}$$

Thus, the Lagrangian becomes

$$\mathcal{L} = \frac{1}{2}[(\partial_\mu - iqA_\mu)\phi^*][(\partial^\mu + iqA^\mu)\phi] - V(\phi^*\phi) - \frac{1}{4}F^{\mu\nu}F_{\mu\nu} \tag{2.6}$$

where
$V(\phi^*\phi) = \frac{1}{4}\lambda^2(\phi^*\phi)^2 - \frac{1}{2}\mu^2(\phi^*\phi)$
$F_{\mu\nu} = \partial_\mu A_\nu - \partial_\nu A_\mu$.

The minima of the potential function

$$\begin{aligned} V(\phi^*\phi) &= \frac{1}{4}\lambda^2(\phi^*\phi)^2 - \frac{1}{2}\mu^2(\phi^*\phi) && (2.7)\\ &= \frac{1}{4}\lambda^2(\phi_1^2 + \phi_2^2)^2 - \frac{1}{2}\mu^2(\phi_1^2 + \phi_2^2) && (2.8) \end{aligned}$$

is represented by a circle with radius $\frac{\mu}{\lambda}$

$$\phi_{1min}^2 + \phi_{2min}^2 = \frac{\mu^2}{\lambda^2}. \tag{2.9}$$

There are thus an infinite number of vacuum states. In order to break the symmetry of the gauge group, the field needs to be expanded around a chosen vacuum.

Studying the potential $V(\phi^*\phi)$, if μ^2 is positive, the potential has only one vacuum state at

$$\phi = 0.$$

If μ^2 is negative, the potential has a vacuum state at

$$|\phi| = \sqrt{\tfrac{|\mu^2|}{2\lambda}}$$

It is this vev that breaks the U(1) symmetry, as seen below.
Re-writing ϕ to be:

$$\phi = \frac{1}{\sqrt{2}}e^{i\frac{\chi}{\nu}}(\nu + h) \tag{2.10}$$

where χ and h are real fields, and ν is defined by

$$\begin{aligned} \frac{\nu}{\sqrt{2}} &= \sqrt{\frac{|\mu^2|}{2\lambda}} && (2.11)\\ &= \sqrt{\frac{-\mu^2}{2\lambda}}. && (2.12) \end{aligned}$$

Substituting this into the Lagrangian of Eqn. 2.6 will result in interaction terms that do not have any real direct physical meaning. These are the result of the production of a massless Goldstone boson (χ) from the broken symmetry. A suitable choice of gauge eliminates the Goldstone boson, leaving a single massive scalar field (h), the Higgs field, and terms relating to the mass of particles.

The above described BEH mechanism can now be applied to the electroweak theory. This model has four gauge bosons, W^i_μ and B_μ, which will correspond to the $W^\pm$, Z^0, and photon. The kinetic energy term in the Lagrangian is

$$\mathcal{L}_{KE} = -\frac{1}{4}W^i_{\mu\nu}W^{\mu\nu i} - -\frac{1}{4}B_{\mu\nu}B^{\mu\nu} \tag{2.13}$$

where

$$W^i_{\mu\nu} = \partial_\nu W^i_\mu - \partial_\mu W^i_\nu + g\epsilon^{ijk}W^j_\nu W^k_\nu \tag{2.14}$$

$$B_{\mu\nu} = \partial_\nu B_\mu - \partial_\mu B_\nu. \tag{2.15}$$

We apply the same method as above, and choose the vev of ϕ to be

$$< \phi >= \begin{pmatrix} 0 \\ \frac{\nu}{\sqrt{2}} \end{pmatrix}. \tag{2.16}$$

Like the above, by choosing a suitable gauge, the Goldstone boson will be removed while the Higgs scalar will still remain. Because of this term in the Lagrangian, the boson masses can be obtained. The real fields are produced to be

$$W^\pm_\mu = \frac{1}{\sqrt{2}}(W^1_\mu \mp iW^2_\mu) \tag{2.17}$$

$$Z_\mu = \frac{-g'B_\mu + gW^3_\mu}{\sqrt{g^2 + g'^2}} \tag{2.18}$$

$$A_\mu = \frac{gB_\mu + g'W^3_\mu}{\sqrt{g^2 + g'^2}} \tag{2.19}$$

and through the BEH mechanism, their masses are

$$M^2_W = \frac{1}{4}g^2\nu^2 \tag{2.20}$$

$$M^2_Z = \frac{1}{4}(g^2 + g'^2)\nu^2 \tag{2.21}$$

$$M_A = 0. \tag{2.22}$$

The calculated values for the masses were

$$M_W = 82 \pm 2 \text{ GeV}$$
$$M_Z = 92 \pm 2 \text{ GeV}.$$

Through experiments performed at CERN, the mass of the W and Z bosons were found to be 80.41±0.18 GeV and 91.1884±0.0022 GeV, respectively [19, 20].

2.2 Beyond the Standard Model

The SM to this date has been successfully proven by experiments, however it is not a complete theory in describing nature. Some of the shortcomings of the SM [21, 22] include:

- Gravity is excluded from this theory.
- Descriptions at the electroweak symmetry breaking scale (246 GeV) is quite accurate, but the SM fails at energies above the Planck scale ($\sim 10^{19}$ GeV) where gravity cannot be ignored.
- There are 19 arbitrary parameters. Their values are determined from experiment but the SM does not explain why the parameters have those values.
- There is no candidate for dark matter in the theory. Dark matter makes up about 26% of all the matter in the Universe, whereas known matter only makes up 4% of the content of the Universe [23].

Beyond the Standard Model (BSM) theories have thus been constructed in an attempt to explain what the SM cannot about nature. Many of these BSM models predict the existence of heavy bosons with spin-1, and thus their production in experiments could be an indication for new physics [24]. One of the bosons postulated by some of the BSM theories is the Z' boson, and below is a description on some of these models.

Extension of the Standard Model to include a $U(1)'$

An extension of the SM gauge structure which includes a second $U(1)$ group

$$SU(3)_C \otimes SU(2)_L \otimes U(1)_Y \otimes U(1)'$$

gives the associated Z' gauge boson which is electrically neutral with spin-1. The spontaneously broken $U(1)'$ gauge symmetry leads to the massive Z' boson. This symmetry is broken at a scale much larger than the electroweak scale. Grand Unified theories (GUT's), such as SO(10) and E_6, as well as superstring theory naturally predict the existence of the broken $U(1)'$ gauge symmetry [25].

E_6 Model

This model contains two Z' bosons, which can mix. The decomposition of the E_6 GUT results in two extra $U(1)'$

$$E_6 \rightarrow SO(10) \otimes U(1)_\psi \rightarrow SU(5) \otimes U(1)_\chi \otimes U(1)_\psi$$

The $SU(5)$ breaks to the SM gauge symmetry and a $U(1)_\theta$ which is a linear combination of $U(1)_\chi$ and $U(1)_\psi$. The neutral gauge bosons that correspond to the $U(1)_\chi$ and $U(1)_\psi$ are Z'_χ and Z'_ψ. Their combination gives the form of a Z' boson that is a result of the mixing of the $U(1)'$:

$$Z'(\theta) = Z'_\psi cos(\theta) + Z'_\chi sin(\theta) \tag{2.23}$$

where the θ in Eqn. 2.23 is the mixing angle [26–28].

Left-Right Symmetric Model (LRM)

The LRM has the low-energy gauge group

$$SU(2)_L \otimes SU(2)_R \otimes U(1)_{B-L}$$

where B and L are baryon and lepton numbers, respectively. This electroweak gauge group symmetry arises from either an $SO(10)$ or E_6 GUT. There is both a Z' and a new charged $W_R^\pm$ gauge boson due to the presence of the $SU(2)$. In this model, the mass ratio of the W' and Z' is given by

$$\frac{M_{Z'}^2}{M_{W'}^2} > 1.$$

The existence of a $W' = W_R$ with the correct mass ratio to the Z' can test the performance of this model [26, 27].

Little Higgs Model

This model contains new gauge bosons: Z' and W' bosons at the TeV scale to remove the Higgs mass quadratic divergences from the SM gauge bosons. The heavy gauge bosons are the result of broken generators produced from global symmetry breaking in the extended gauge sector of the Little Higgs Model [26, 27].

The Sequential Standard Model

The sequential Z'_{SM} boson has the same couplings to fermions as those of the SM Z boson, only it is heavier. This model is not gauge invariant, but it serves as a useful reference when comparing constraints from various sources, and is a benchmark in experimental Z' searches at the LHC [26, 27].

Chapter 3

Experimental Apparatus

3.1 The Large Hadron Collider

The LHC[1] is a particle accelerator ring with a circumference of 27 km, and it is built about 100 m underground at the CERN laboratory in Geneva, Switzerland. This particle accelerator collides together beams of protons or beams of lead ions travelling close to the speed of light, and from their collisions, we are able to discover and study the fundamental particles that make up the Universe. The LHC consists of the main 27 km ring of superconducting magnets which guide the proton beams around the ring, as well as a few smaller accelerating structures that increase the energy of the particles before they collide in the main LHC ring. Figure 3.1 shows the structures through which the particles must travel in the LHC. The first series of particle acceleration begins in the linear particle accelerator (LINAC 2) which generates 50 MeV protons. These protons are then injected into the Proton Synchrotron Booster (PSB) which accelerates the particles to 1.4 GeV, and then they are accelerated in the Proton Synchrotron to 26 GeV. Finally, the Super Proton Synchrotron (SPS) increases the proton-energy to 450 GeV before they are at last fed into the main ring. In the main accelerator during 2012, the proton beams were accelerated to a maximum centre-of-mass energy $\sqrt{s} = 8$ TeV (4 TeV per beam), and were directed around the ring by the strong magnetic fields generated by superconducting electromagnets. Magnets of different sizes and types are used to focus the proton beams and to force the particles closer together so that the probability of successful collisions increases. The proton beams in the LHC are controlled to collide at the four particle detectors: ATLAS, CMS, ALICE, and LHCb. By the end of the shutdown period of the LHC, in 2015, the centre-of-mass energy will be increased to 13 TeV or 14 TeV.

[1]Material for this section has been extracted from Reference [29].

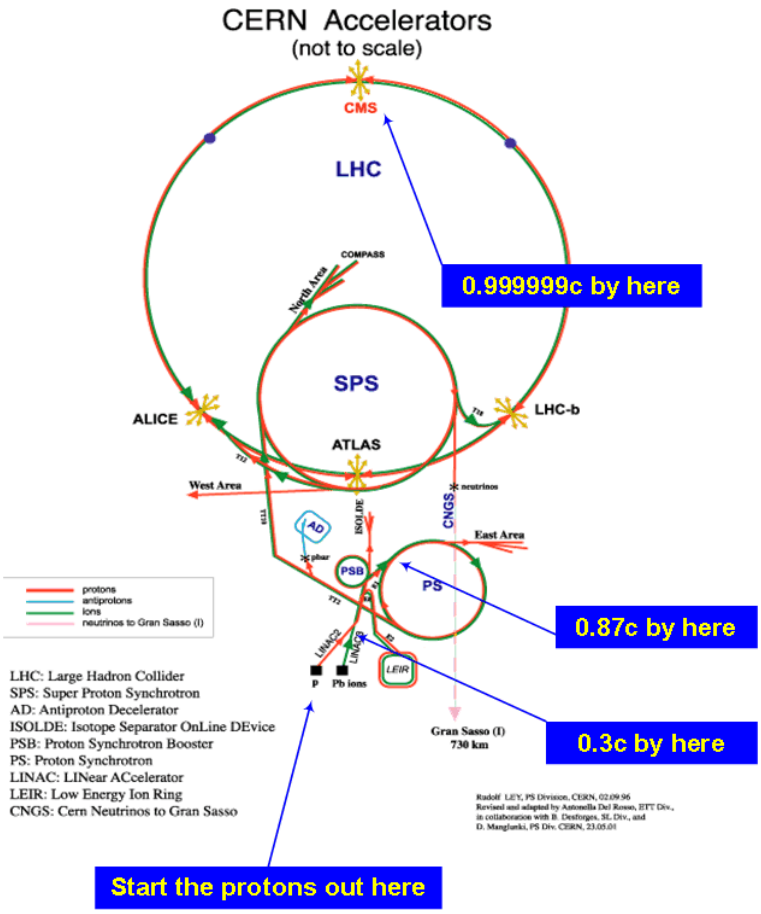

Figure 3.1: Layout of the CERN accelerator complex, including the LHC [30].

3.2 The ATLAS Detector

The ATLAS detector[2], as shown in Figure 3.2, is one of the general purpose detectors at the LHC at CERN. It focuses on the search for the origins of mass, extra dimensions, microscopic black holes, dark matter, as well as particles beyond the SM, such as the hypothetical Z' boson. The ATLAS detector is 45 m long, 25 m high and weighs about 7000 tons. The detector is made up of specific components which allow for the identification of the known particles, and measurements of their energy and momentum. The high collision rate between proton beams in the detector generates a massive data-flow, and to be able to record these data, ATLAS uses a highly advanced trigger and data acquisition system, and a large computing system.

The co-ordinate system, shown in Figure 3.3, used to describe the ATLAS detector and the particle collisions, is chosen so that the interaction point defines the origin, the beam direction defines the z-axis and the x-y plane is perpendicular to the beam axis. The positive

[2]Material for this section has been extracted from Reference [1].

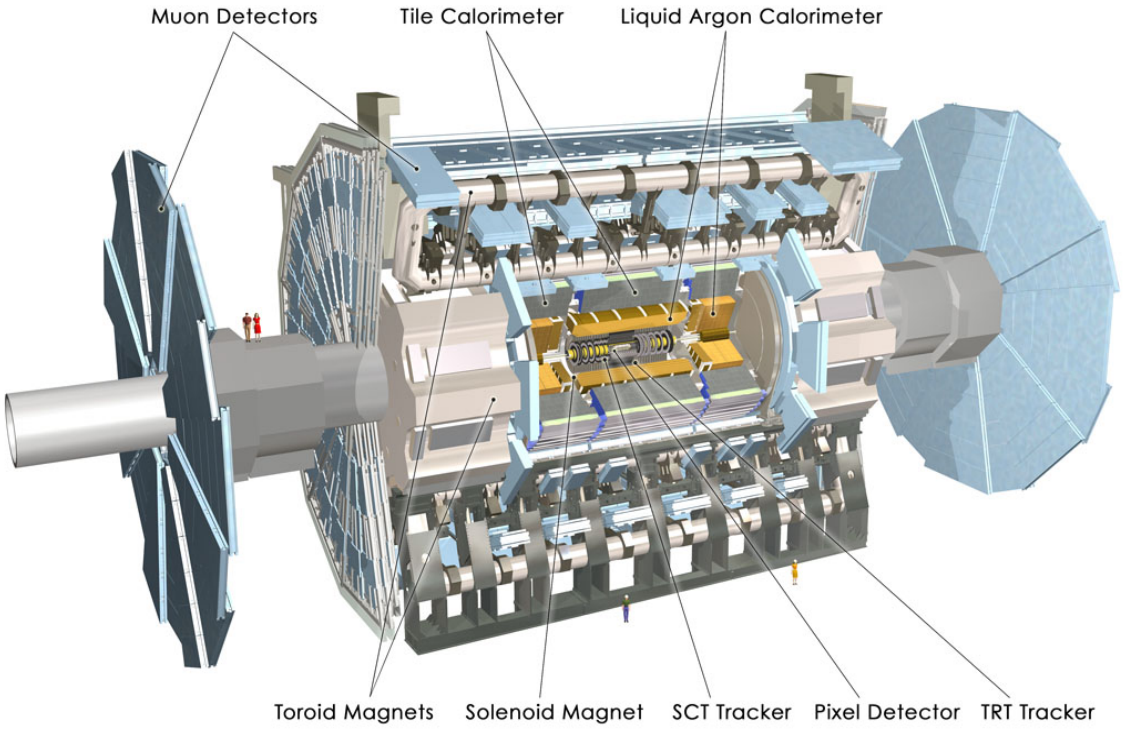

Figure 3.2: The ATLAS Detector [31].

x-axis points from the interaction point to the centre of the LHC ring, and the positive y-axis points upwards.

The azimuthal scattering angle ϕ is measured around the beam axis, and the polar angle θ is measured from the beam axis. To describe the positions of particles in the detector, the pseudorapidity η is required, where η is defined as

$$\eta = -\ln[\tan(\frac{\theta}{2})] \tag{3.1}$$

The position of a particle is represented by a point in η-ϕ plane. The separation distance ΔR between two close-lying tracks is defined as

$$\Delta R = \sqrt{\Delta\eta^2 + \Delta\phi^2}. \tag{3.2}$$

The p_T, transverse energy E_T, and the missing transverse energy E_T^{miss} are defined in the x-y plane. Missing energy arises if there is an imbalance in the vector sum of the p_T. The initial direction of the colliding beams is along the beam direction, thus the initial energy in the transverse plane is zero, but if it is not, then missing energy is present [33].

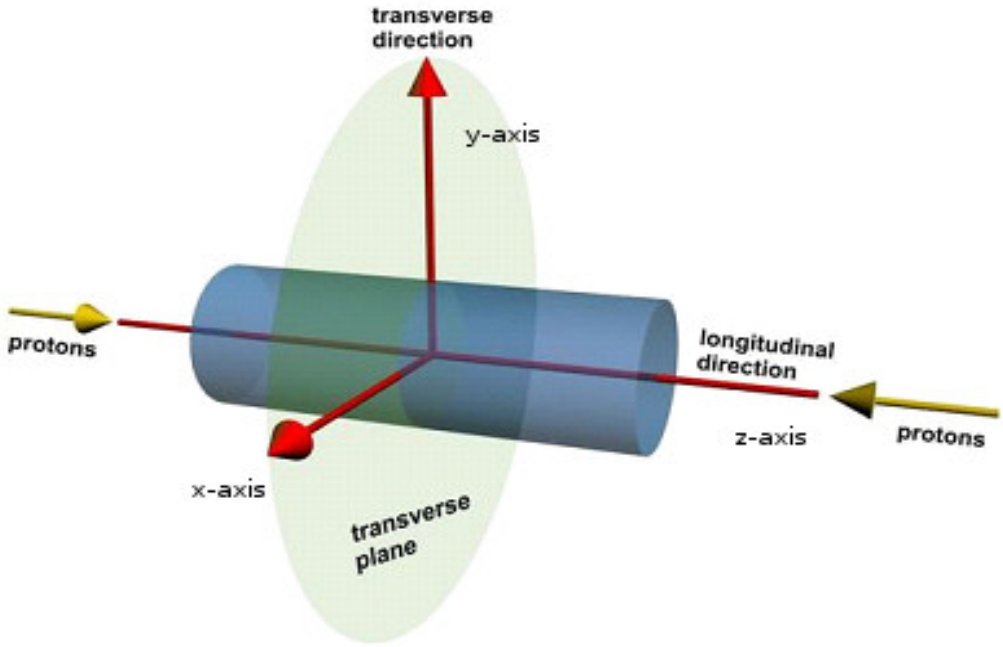

Figure 3.3: The ATLAS co-ordinate system [32].

ATLAS is made up of different layers of components each with its own ability to detect specific properties, or types of particles, as shown in Figure 3.4. The inner detector forms the innermost layer, and its purpose is to track the paths of charged particles, such as electrons, protons and muons, and measure their p_T as well as to provide high-precision tracking information for them. Neutrons and photons are neutral particles, thus they do not leave tracks in the tracking chamber. The inner detector is influenced by a magnetic field of 2 T generated by the central solenoid, and it has three sub-systems: the high resolution silicon Pixel detector, the Semi-Conductor Tracker (SCT) and the Transition Radiation Tracker (TRT). The first two subsystems cover a region of $|\eta| < 2.5$ and the TRT covers a region of $|\eta| = 2.0$. Moving outwards from the inner detector are the electromagnetic (EM) and the hadronic calorimeters. They measure the energies of charged and neutral particles, and they cover a pseudorapidity range of $|\eta| < 4.9$. The calorimeters are made to be very dense so that the hadronic and electromagnetic showers do not pass through into the muon detection system. The muon spectrometer surrounds the calorimeter since muons are the only detectable particles that can pass through the calorimeter without being stopped. The spectrometer measures muons' trajectories and their momenta by deflecting them as they traverse through the magnetic field generated by the superconducting toroid magnets. Monitored Drift Tubes (MDT) measure, with high precision, the position of the muons as they pass through. Cathode Strip chambers (CSC) provide the same function as the MDT, but they offer a finer granularity because they cover the pseudorapidity range $2.0 < |\eta| < 2.7$, which is the region of high particle rate.

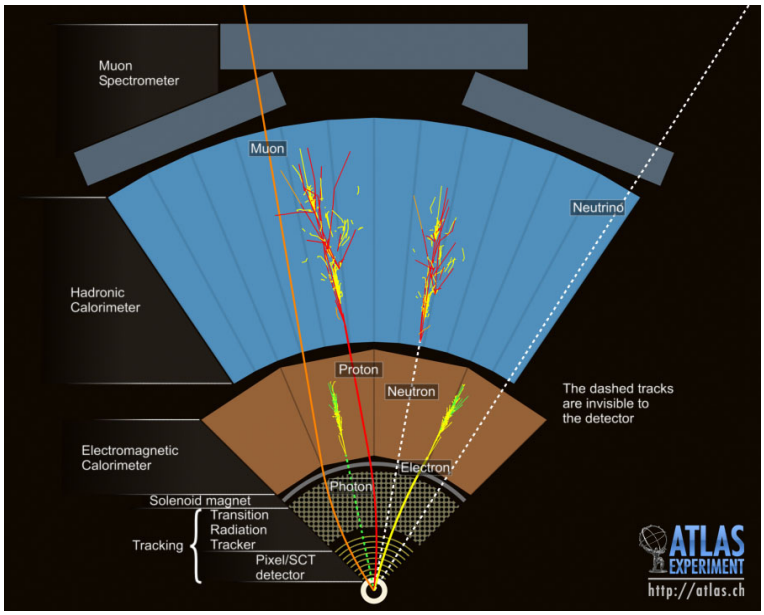

Figure 3.4: The different particles interact differently with the various layers of the ATLAS detector so that they can be identified and measured [34].

The detector is unable to detect neutrinos because they do not interact with the detector material. Their presence from a collision is inferred from detecting E_T^{miss} in the events.

The folowing sections discuss in more detail each sub-detector of ATLAS, beginning from the innermost layer and proceeding outwards, as well as the trigger system used.

3.2.1 The Inner Detector

The inner detector measures the p_T of each charged particle. It is made up of three detector types: the high resolution silicon Pixel detector in the inner radii, the Semi-Conductor Tracker (SCT) and the Transition Radiation Tracker (TRT) in the outer radii, as shown in Figure 3.5. All these components sit in a magnetic field of 2 T generated by the Central Solenoid. All the inner detector components contribute to the precise measurement of the charged particle tracks, but each component has its own unique function. The Semi-Conductor Pixel detector, followed by a silicon micro-strip detector, measures the vertex region with high accuracy and offers high granularity for excellent pattern recognition. The point where particles are produced is the vertex. It is not only the collision of two beams that give rise to particles, but also through particle decay and particle interaction with the material of the detector. The Semi-Conductor Tracker (SCT) measures the momenta of the particles, the impact parameter, and the vertex position with precision, and the Transition Radiation Tracker (TRT) ensures continuous tracking to enhance pattern recognition, improves momentum resolution and allows for the detection of transition radiation hits in the

outer part. Transition radiation is produced when very high energy particles travel through materials of different electrical properties. Particle identification is made possible because the intensity of the transition radiation is approximately proportional to the energy of the particle [35]. The TRT is used to identify electrons, and it uses gaseous straw detectors. The TRT is able to perform the above functions because it has an average of 36 hits per track, and 420 000 channels that are read out.

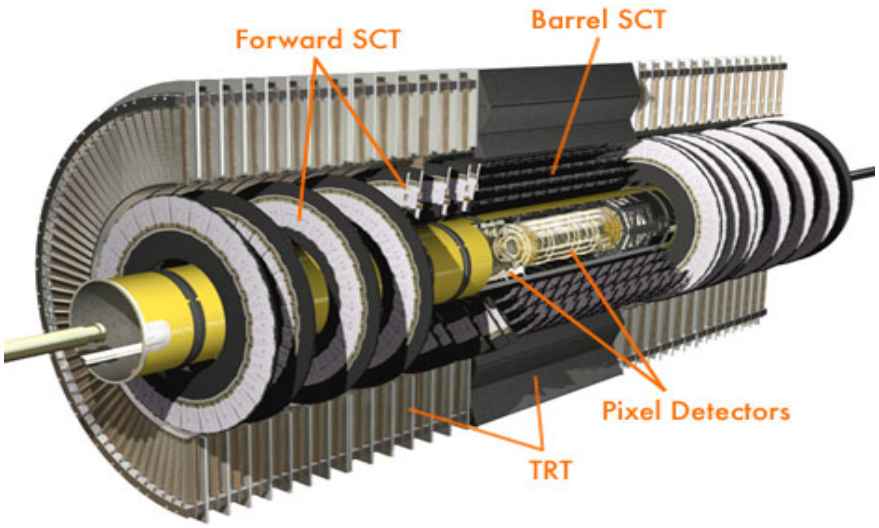

Figure 3.5: Inner detector and its components [36].

3.2.2 The Calorimeters

The calorimeter measures the charged and neutral particle energies. It is made of metal sheet absorbers and sensing elements. When particles interact with the absorber, a shower of secondary particles are produced which are then detected by the sensing elements. Since both electromagnetic showers and hadronic showers are produced, the calorimeter consists of an electromagnetic calorimeter and a hadronic calorimeter. These sub-detectors cover a pseudorapidity range of $|\eta| < 4.9$, and are made to be very thick so that the hadronic and electromagnetic showers do not pass through into the muon detection system.
Electromagnetic showers are secondary particles that are produced when particles such as photons and electrons, which interact via the electromagnetic force, make contact with matter. Hadronic showers are the result of hadrons interacting with matter. The hadrons, such as protons, neutrons or pions, are composed of quarks and thus interact through the strong force. The showers continue to be produced through the interaction of the particles with matter until the average energy per particle is too low to produce any more particles.

Electromagnetic calorimeters are made of lead absorbers in an accordion geometry, and the sensing element used to collect signals is liquid argon. The accordion shape is used so that

there is a full coverage in ϕ without any cracks. Between the layers of lead absorbers is liquid argon, and the small gap that is filled with liquid argon is maintained under a strong electric field. When electrons or photons interact with the lead absorbers, they lose energy which results in the production of a shower of secondary particles. These particles then ionise the argon atoms. Due to the electric field, the ionised electrons drift through the liquid argon to copper electrodes which are placed between two consecutive absorbers. At the electrodes, the electrical current that is generated is proportional to the deposited energy. The resultant signal is amplified, shaped, digitized, then recorded. From the information obtained, the original energy of the particle that entered the calorimeter can be calculated. Electromagnetic calorimeters offer high granularity which allows for the precise measurements of position and energy of electrons and photons. They cover the pseudorapidity range $|\eta| < 3.2$.

The Tile Calorimeter (TileCal), as shown in Figure 3.6, is a hadronic calorimeter which is made of steel absorbers, and the sensing elements are scintillating plastic tiles. Hadronic calorimeters have coarser granularity which is sufficient for the reconstruction of jets. Since this dissertation focuses on hadronic particles, there will be a more detailed discussion regarding the TileCal detector. Preliminary results showing measurements of the light distribution in the scintillation counters will also be shown in Chapter 4.

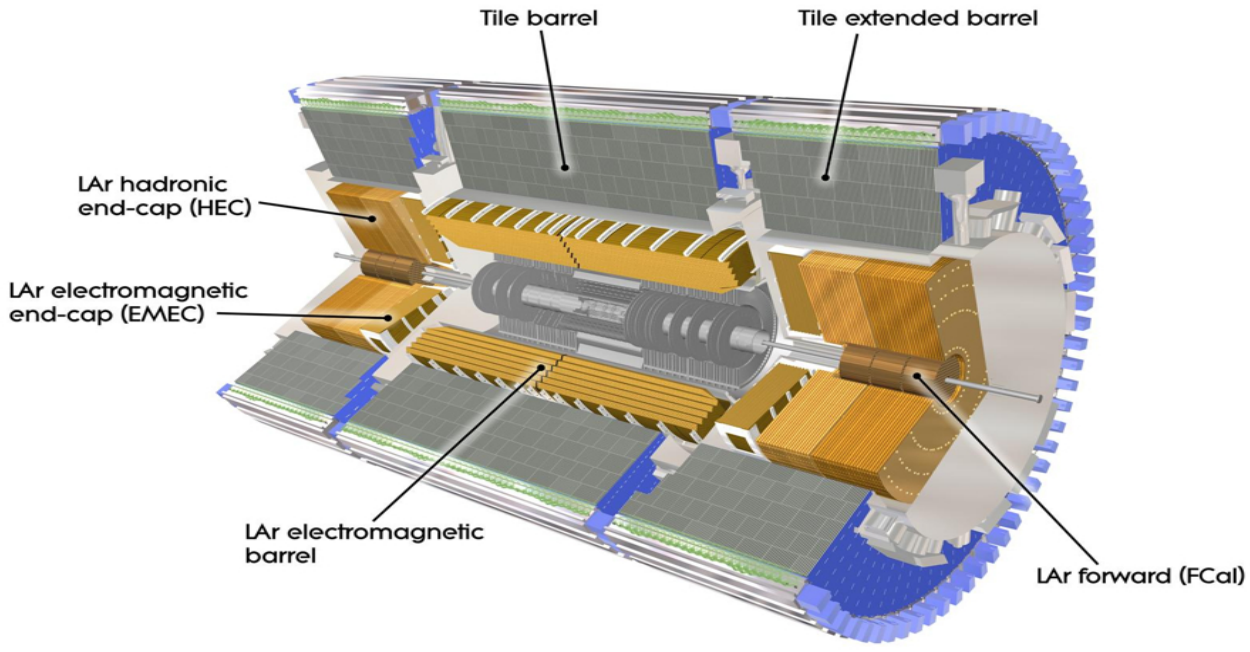

Figure 3.6: A part of the ATLAS detector, showing the hadronic calorimeters and the EM calorimeters [1].

Many of the physics searches at the ATLAS experiment rely on the precise identification and reconstruction of jets [37]. Since multijets are one of the dominant backgrounds in most

new particle searches, it is important to be able to efficiently reconstruct jets so that this type of background can be rejected. TileCal measures accurately the energy and position of electrons, photons, isolated hadrons, taus and jets. It thus performs an important role in the identification of several particles in both the SM and BSM searches.

This calorimeter is composed of a large central barrel which is flanked on either side by two smaller extended barrels. Each barrel consists of 64 modules which are made of steel plates and scintillating tiles. The steel plates are fitted together to form slots in which the scintillating tiles are inserted. Two wavelength shifting (WLS) fibers on both edges of each tile collect the light produced by the ionizing particles traversing and showering in the calorimeter. The fibers from each tile edge are then gathered together and coupled to two different photomultipliers (PMTs) positioned at the outer edge of each module. The purpose of using two PMTs is to ensure a redundant readout for the signal of each cell so that the reliability of the TileCal is enhanced. The uniformity of the signal when summed is also improved [37]. If only one PMT were read out the response non-uniformity, caused by light attenuation in the scintillating tiles, would be up to 40% [38]. Studies have shown that the acceptable level of the overall response non-uniformity has to be no more than 10% [39]. To achieve this value, the non-uniformity inside the tile must be below 5%. Figure 3.7 shows the module consisting of the alternating steel-scintillator arrangement, as well as the WLS fibers coupled to the PMT.

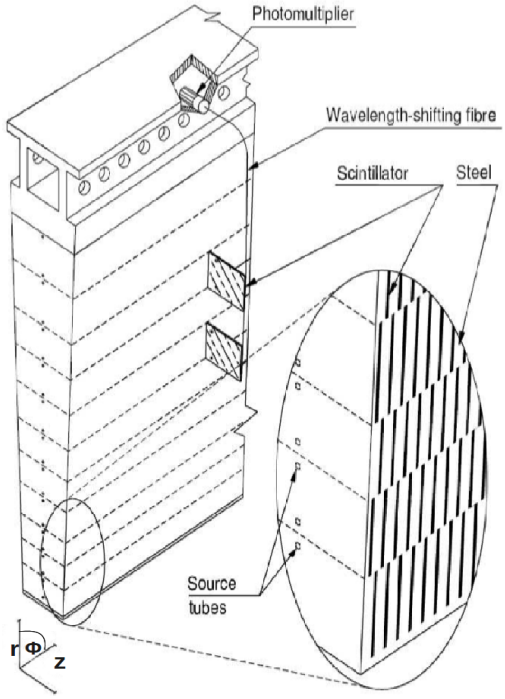

Figure 3.7: The TileCal module [38].

In the gap region between the central barrel and the extended barrel which is required for services and cables, thin scintillation counters are installed so that energy lost in this region can be partially recovered [37]. Such counters have the names: E1, E2, E3 and E4. Figure 3.8 shows the position of the scintillation counters in the gap region. E3 and E4 scintillation counters are known as the crack scintillators and they extend into the transition region between the barrel and endcap EM calorimeters. These crack scintillators have the purpose of measuring the energy of the EM showers that are produced when the incoming particles interact with the dead material of the cryostat walls of the EM calorimeter and with the inner detector cables [40]. It is important then to have a uniform light response in the E3 and E4 scintillation counters to ensure a good energy resolution of the incoming particles.

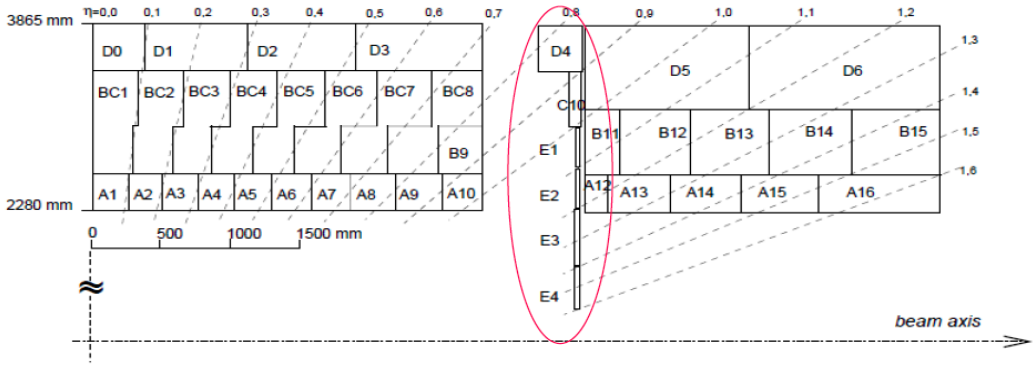

Figure 3.8: The position of the scintillation counters in the gap region [38].

3.2.3 The Muon Spectrometer

The muon spectrometer shown in Figure 3.9 surrounds the calorimeter since muons are the only detectable particles that can pass through the calorimeter without being stopped. The spectrometer not only measures the muon's trajectory and determines its momenta in the pseudorapidity range $|\eta| < 2.7$, it also serves as a trigger to select the events with high energy muons. The measurements all occur inside a volume of magnetic field generated by superconducting toroid magnets. Muon tracks are thus deflected by this magnetic field, and this allows the momenta of the muons to be calculated from their bent trajectories. The muon spectrometer consists of Monitored Drift Tube (MDT) chambers which contain many metal tubes that are filled with gas, and each tube has a wire running through its centre. As the muons travel through the gas, ionisation takes place to produce electrically charged ions and electrons which drift towards the sides of the tube and the wire. The position of the muon as it passes through the tube can then be determined with precision by measuring the time it takes for the charges to drift from their starting point. Cathode Strip chambers (CSC) are multiwire proportional chambers with cathode planes segmented into strips. Similar to what happens in the MDT, as muons pass through the gas ionisation takes place. The positive ions drift towards the cathodes while the negative ions drift towards the wire. The wire signals are not read out. The position of the track is obtained by looking at charges induced on neighbouring cathode strips. The CSC offers finer granularity than does the MDT, and thus allows them to be used to determine the muon trajectory in the forward region which, compared to the barrel region, contains a higher track density. The trigger system covers the pseudorapidity range $|\eta| < 2.4$, and is composed of the Resistive Plate Chamber (RPC) and the Thin Gap Chamber (TGC). The RPC is a gaseous electrode-plate detector with no wires. Two parallel resistive plates are separated by a 2 mm gap which is filled with a gas mixture. As the particles traverse through the gas, ionisation takes place which induces a signal that is then read out by metallic strips mounted on the outer face of the resistive plates. The RPC is used in the barrel region because it offers good spatial and time resolution. In the end-cap regions, the TGC is used which provides good time resolution and high rate capability. The TGC is a multiwire proportional chamber and thus operates on the same principle as the CSC.

As muons traverse through the calorimeter and materials of the muon spectrometer, they lose very little of their energy.

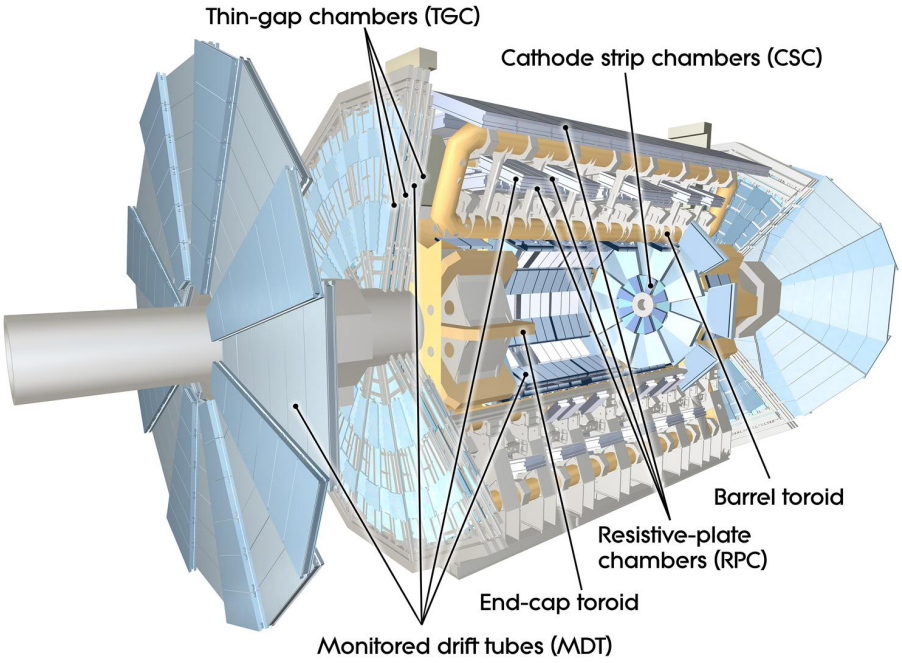

Figure 3.9: The muon system [1].

3.2.4 The Trigger System

An efficient trigger system to just select the interesting events is required because approximately 1000 particles will be produced every 50 ns from the collision point, and it is not technologically possible at the moment to record all the events. An event is regarded as interesting if it allows for the evaluation of predicted event signatures. A trigger is a combination of electronic components that provide fast signal when an interesting event has taken place. The trigger system works with the information generated by the different components of the ATLAS detector. There are three levels of the ATLAS trigger system: L1, L2, and the event filter. The L1 trigger is hardware-based and searches for signatures from high p_T muons, electrons, photons, jets, and τ leptons decaying into hadrons, as well as events with large E_T^{miss}, and large total E_T. The L1 trigger thus works on a subset of information from the muon spectrometer for high p_T muons, and the calorimeter for electromagnetic showers, jets, τ leptons, E_T^{miss}, and large p_T. This trigger selects the region of interest (RoI) which contains possible trigger objects within an event. The next level is the L2 trigger which further analyses the events in the RoI. This level uses the information from all the detectors for the analysis, and this refines the selection of possible candidate events in the region of interest. The amount of data that is transferred and read out is thus reduced, and this accommodates for the fact that the current technology cannot record all the events. Finally, the event filter (EF) level uses offline reconstruction methods on the complete event information to further select events down to a rate that can be stored for offline analysis. At L1, the event rate is about 75 kHz, and the L2 and EF trigger rate is reduced to about

600 Hz.

Depending on the object being triggered upon, trigger efficiency is dependent on pileup. Pileup are background signals produced from multiple proton-proton collisions during a single bunch crossing in the detector [35]. As the centre-of-mass energy and luminosity increases, pileup will also increase, and the trigger efficiency will be degraded [41]. Methods have to be implemented to improve the trigger efficiency in the high pile-up environment. From 2015, the LHC will run at a centre-of-mass energy close to 13 TeV or 14 TeV. Pileup will increase, but so too will the ability to search for the interesting BSM signal events.

Chapter 4

The Tile Calorimeter Studies

This chapter is dedicated to the discussion of the experiment performed on the scintillation counters of the ATLAS Tile Calorimeter (TileCal). The aim of the experiment was to measure the light collection uniformity and response of the E3 and E4 scintillation counters using Strontium-90 (Sr90) β source.

In order to study the light collection characteristics of the tiles, a Sr90 β source was placed at different positions above the tile's surface. Surrounding the tile is a sheet of Aluminium (Al) casing to protect the tile from damage. Al tapes around the edges of the casing secure the casing. The light from the interaction between the source and the scintillating tile was collected by the WLS fibers and registered by the PMT and associated electronics. The set up, in B175 at CERN, that was used for the study is shown in Figure 4.1.

Figure 4.1: The Sr90 laboratory consists of the light-tight scanbox, control crate, multimeter and data acquisition PC [42].

Referring to Figure 4.2 below, Sr90 β source was used and it emitted 0.5 MeV electrons which were the ionising particles. The source scanned the surface of the counters in two directions in 1 mm steps, and this generated a 2D light response map. As electrons traverse through the polystyrene material of the 6 mm E3/E4 scintillator tiles, they excite the molecules which would in turn excite the primary dopant (PTP). This induces the production of light in the ultraviolet range. These short wavelength photons interact with a secondary dopant (POPOP), and light of a longer wavelength is produced. This scintillation light propagates through the tile and reflects off its surfaces. If the angle of reflection is greater than 38.9^0 (the critical angle), some of the light will refract out the tile. In order to reduce the chance of this happening, the tiles were wrapped in Tyvek paper because the irregular surface of this paper increases the probability of internal reflection. As the light travels through the scintillator and towards the tile edge, its intensity attenuates exponentially. Once at the tile edge, the light is absorbed by WLS fibers which increases its wavelength further, and the light propagates to the PMT. The end of the fiber away from the PMT is aluminized to reflect any light impinging on it towards the PMT. This helped to increase the light yield [42].

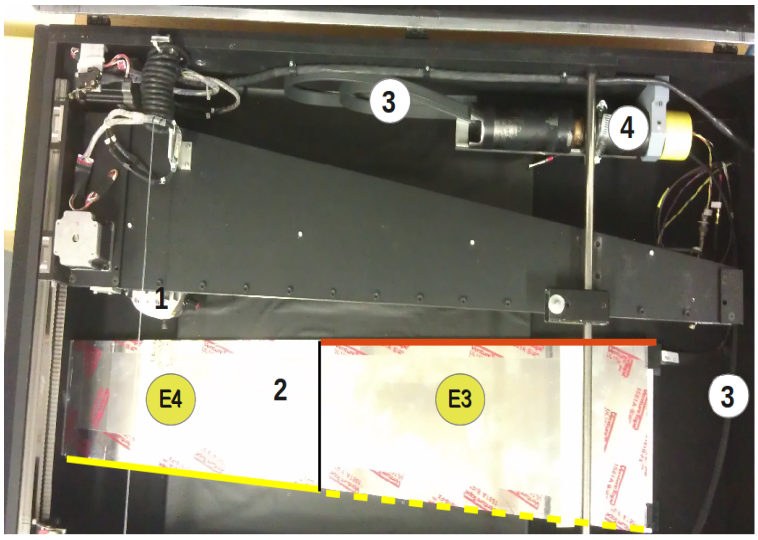

Figure 4.2: Setup showing the Sr90 source (1), E3/E4 scintillator tile (2), WLS fibers (3), and the PMT(4). The E3 and E4 scintillator tiles are shown together with the arrangement of their WLS fibers.

Figure 4.2 shows a scintillation counter in the light-tight scanbox. 6 WLS fibers were coupled to the E3 scintillator and 6 WLS fibers were coupled to the E4 scintillator to measure the light distribution in each of the scintillator tiles. Figure 4.2 shows how the readout fibers are coupled to the two scintillator tiles. The top red strip represents the E3 read-out fibers, and the bottom yellow strip for the E4. The dashed yellow line indicates the part of the fibers that are outside the Tyvek paper to ensure that only E4 is read out.

The 2D response map shows the result when both the E3 and E4 fibers were read out. These were the first set of measurements.

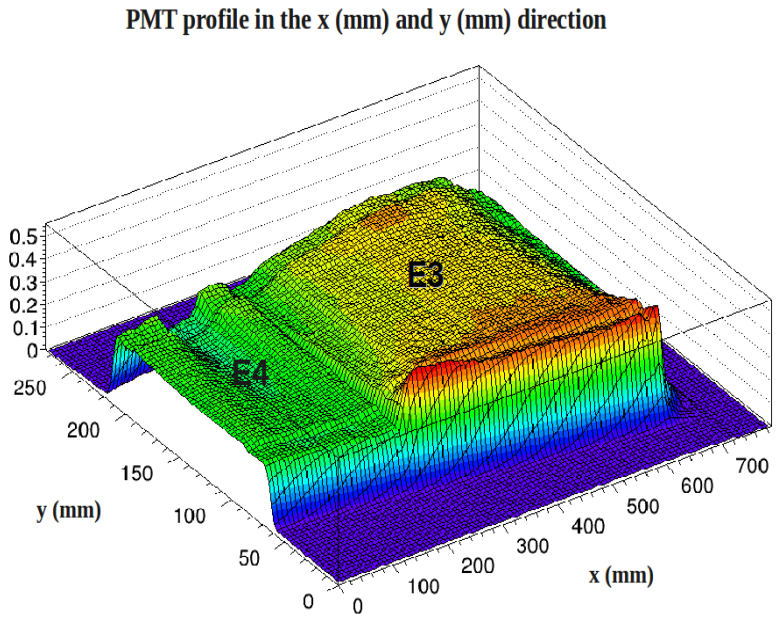

Figure 4.3: 2D response map showing the light distribution in E3 and E4 scintillator tiles of counter number 65.

The high response regions along the x direction, as seen in Figure 4.3, are the read-out fiber sides. There is a dip in the response on the read-out fiber side of the E4 scintillator. This was due to the fact that light escaped through the fibers. Because it had to be ensured that the 6 WLS fibers did not overlap each other and that they coupled to the edges of E3 and E4 scintillator tiles, a piece of green tape was glued over each set of fibers and the light was escaping through the coupling of the fibers to the tape. The high peak at the edge of the read-out fiber side of E3 was caused by the fibers absorbing the primary UV light. The presence of the Al tape was shown as dips around the edges of the response map. The position of the dips coincided with the position of the tape around the Al casing, thus it was concluded that the tape absorbed some of the light which resulted in the reduction of the response. This gave rise to the dips observed in the response map.

The second and third scans were only of the E3 tile with the Al cover and without the Al cover, respectively. Their 2D response maps (Figure 4.4 and Figure 4.5) are compared below. In this report, the results for E4 are not presented because, due to the dimensional constraints of the light-tight scanbox, only about 2/3 of the E4 tile could be scanned.
It can be seen that the response map of E3 with the Al cover gives a more uneven surface compared to E3 without the Al cover. The dips are prominent around the map edges for the first case. The reason for these features are the same as for the above features.

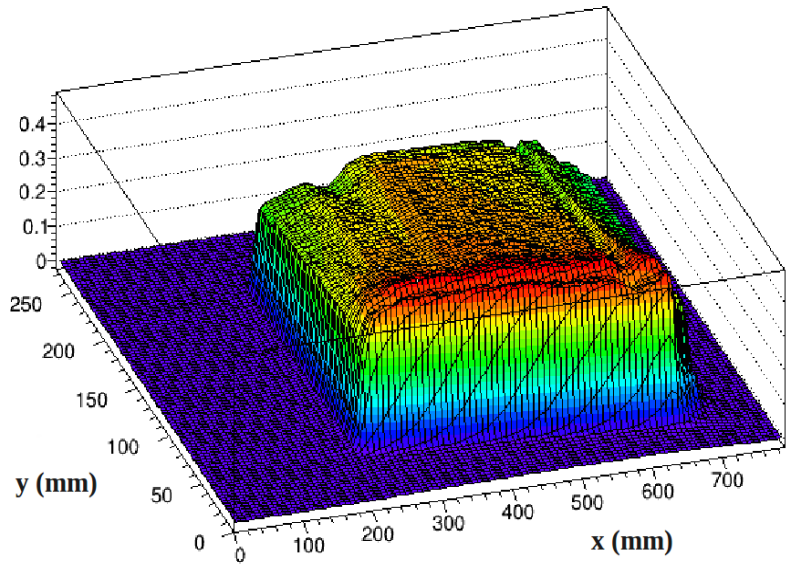

Figure 4.4: 2D response map showing the light distribution in E3 tile with Al cover.

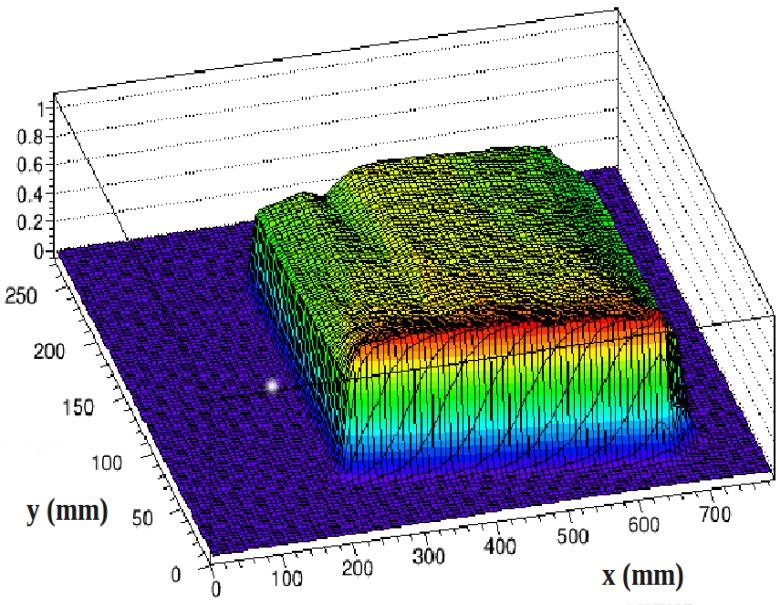

Figure 4.5: 2D response map showing the light distribution in E3 tile without Al cover.

The response non-uniformity can be calculated for the two cases using their respective PMT (photomultiplier) response plots, Figure 4.6 and Figure 4.7. The response non-uniformity was obtained by dividing the root mean square (rms) by the mean obtained from the plots and converting the values to a percentage. The non-uniformity in response for E3 with the Al cover was about 16%, and the response non-uniformity for the other case was about 15%. This comparsion was made as an attempt to characterise the features seen on the response map of E3 with the Al cover. Even though the response non-uniformity for the low energy

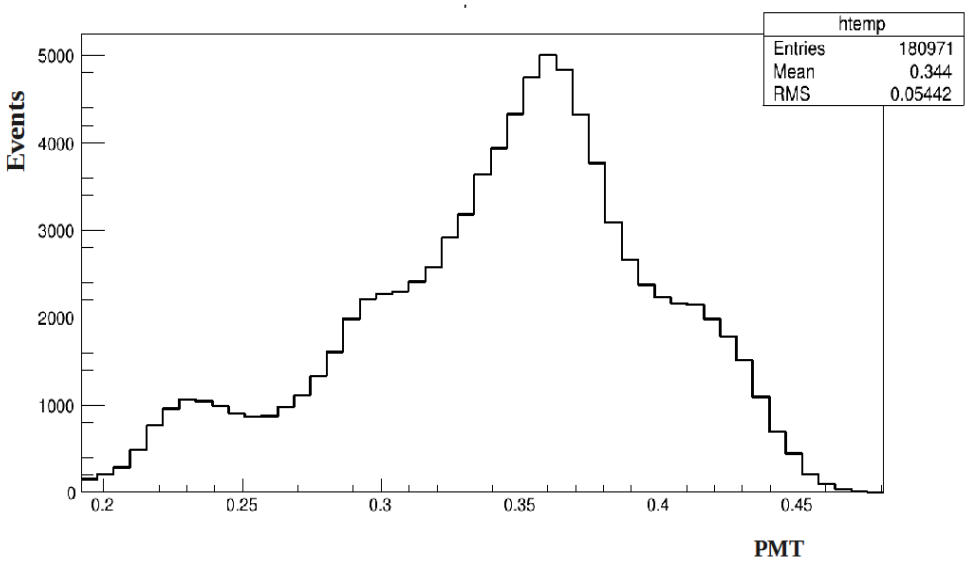

Figure 4.6: The photomultiplier (PMT) response for E3 tile with Al cover.

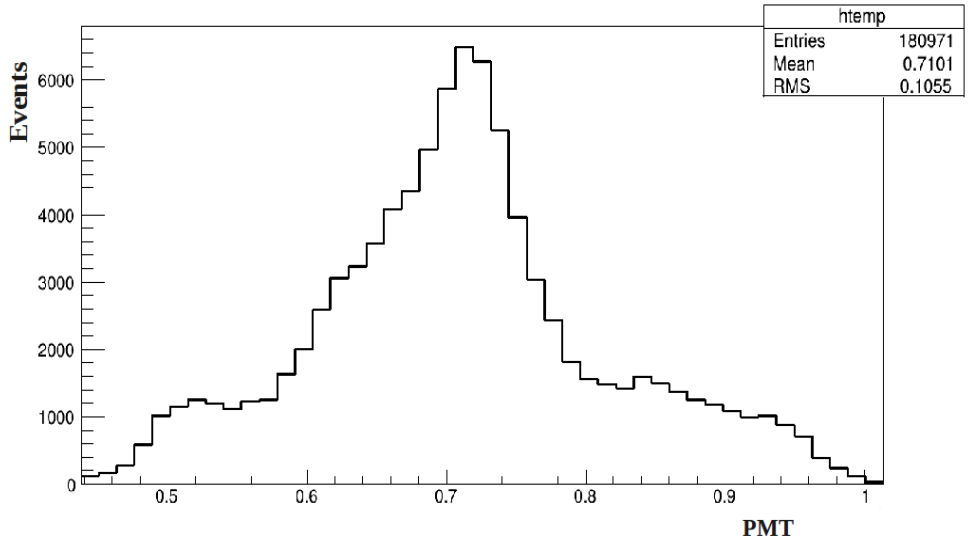

Figure 4.7: The photomultiplier (PMT) response for E3 tile without Al cover.

electrons is higher with the Al cover, the scintillation counters need to be covered by the Al sheet for protection against damage to the tiles.

The Tile Calorimeter is important for the efficient performance of the ATLAS calorimetry which plays a large role in the search for new particles. The response non-uniformity across

the scintillation counters can degrade the performance of the calorimeters, thus in order for the E3 and E4 scintillation counters to ensure a good energy resolution for the dead region of the EM calorimeters and the inner detector, the light response non-uniformity across the E3 and E4 counters must be within the design requirements of 5%. It has been seen, however, that many factors affect the uniformity of the light collection across the counters. The next steps would be to understand further the cause of the features observed in the results and characterise them.

Chapter 5

The Trigger Study and Tau Identification in Dense Environments

This project consists of two parts. The first part investigates the trigger efficiency in the analysis of the heavy Z' boson decaying to hadronic tau pairs, and the second part looks at improving the tau identification (ID) using the tracking.

Triggers used for the analysis impose a specific criteria on the tau candidates to refine the selection, and reduce background contributions. It is necessary to only select events of interest in the data because it is impossible at this time to store all the events. In order to search for the Z' boson decaying to two hadronic taus, it is important to be able to reconstruct tau candidates efficiently using information, such as tracking, from the sub-detectors. The experimental signature of taus decaying hadronically is a tau neutrino and one or three charged pions. The decay is accompanied by one or more neutral pions in about 65% of cases, and rarely by kaons [6]. Hadronic tau decays are thus classified into one-prong decays (decay containing one charged particle), or three-prong decays (decay containing three charged particles). The narrower shower shape of the tau signature also helps to distinguish it from jets [43].

When reconstructing hadronic tau decays, τ_{had}, it is important to use information from all the sub-detectors because in the detector, the signature of hadronic tau decays is similar to the signature of jets and other leptons [41]. The reconstruction algorithm used for τ_{had} begins by considering each jet object as a τ_{had} candidate. Kinematic quantities are then calculated using a refined information of the energy clusters that correspond to each τ_{had} candidate. Information about the object's energy is provided by the calorimeter. Associated to each energy cluster are tracks that have satisfied a specific selection criteria. Information from the tracking detectors and the calorimeter is used as inputs to a Boosted Decision Tree (BDT) to effectively select tau candidates and suppress fake contributions from jets and

light leptons. Then, a pre-defined selection criteria is used, which rely on the output of the multivariate methods, in the analysis level to select the τ_{had} candidates [41].

In the silicon tracking detectors, charged particles strike the individual silicon sensors and are recorded as hits. Many tracks are produced from a collision, especially at high pileup. In dense environments, for example in the multi-prong hadronic decay of a high momentum p_T tau lepton or a jet, tracks will become collimated and if they are very close together then track merging problems may appear. If two tracks are close-lying, it is highly probable that they will pass through the same silicon sensor channel and will be detected as one hit instead of as two hits, leading to fewer tracks reconstructed overall. Hits recorded by the silicon sensors are grouped into clusters, which account for the particles activating the neighbouring sensors, and the clusters form "spacepoints" that are used for track reconstruction. "Spacepoints" represent points in three-dimensional space and tracking algorithms combine them into track candidates [44]. Thus, the track merging problem would cause the reconstruction efficiency for three-prong taus to decrease. Figure 5.1 shows that at high p_T, three-prong taus are often reconstructed as two-prong taus. This is the track merging problem, and these two-prong taus are investigated in Section 5.2.1 for the part of the $Z' \to \tau\tau$ study that aims to improve the tau ID using the tracking.

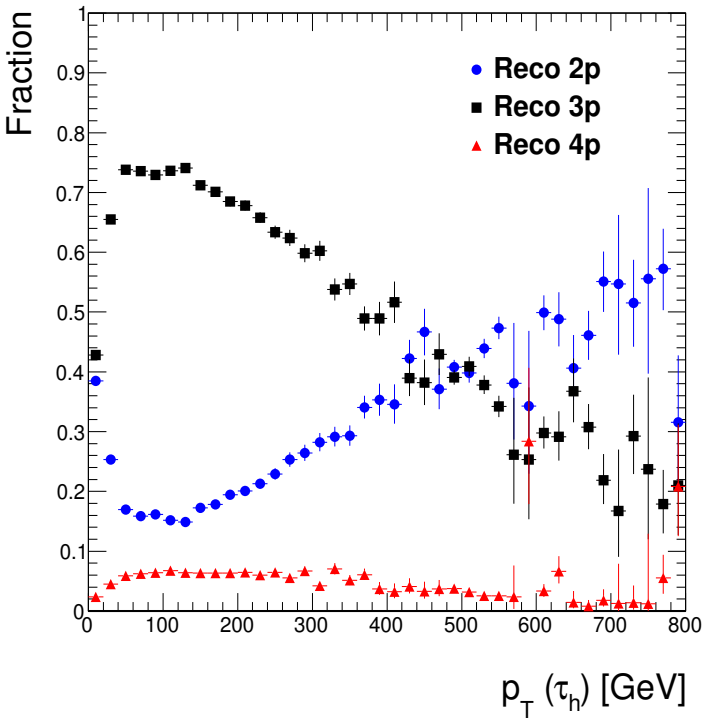

Figure 5.1: At high p_T, the tracks merge giving rise to a higher fraction of reconstructed two-prong tracks instead of three-prongs [43].

Other possible reasons for reconstructing the incorrect number of tracks could be due to the effect of π^0 conversions. Tau decay is accompanied by neutral pions, and photons are emitted from the decay of the neutral pion. The photons will interact with the detector to produce a shower of electrons. If an electron track is detected, it could be considered by the detector to be the second charged track.

The sections that follow will begin with a short discussion of the data and Monte Carlo (MC) samples used, followed by a discussion of the trigger efficiency study and the investigation of improving the tau ID using tracking.

5.1 Data and Monte Carlo Samples

The data used in the search were the 2012 dataset. They were recorded by the ATLAS detector in proton-proton (pp) collisions at a centre-of-mass energy of $\sqrt{s} = 8$ TeV during the 2012 run of the LHC. Only data produced from pp collisions in stable beam conditions were considered, and these data excluded ones that were from the initial running period because there were problems in the simulation of the trigger conditions. The integrated luminosity was thus 19.5 fb^{-1} [43].

The MC sample Drell-Yan $Z/\gamma^\star \to \tau\tau$ was used. It was produced for the study of background, and it was generated with PYTHIA 8.165 [45]. A leading order generator was selected because the sample could then also be re-weighted as Z' signal. The re-weighting procedure is established in Reference [46], and it describes the use of a weighting function that inputs information of the helicity amplitude of a Z' decay and the helicity amplitude of a Drell-Yan process. The weight can be evaluated by comparing the $Z/\gamma^\star \to \tau\tau$ sample reweighted to a Z' sample with the official Z' sample. A "Sophisticated tau decay" option [47] in PYTHIA 8 was used to perform the tau lepton decay.

For the trigger study in Section 5.2, the re-weighted $Z/\gamma^\star \to \tau\tau$ samples were used. These samples were re-weighted to the signal mass of interest, which ranged from 500 GeV - 2250 GeV.

Mass-dependent k-factors were needed to weight the simulated $Z/\gamma^\star$ samples, and were derived from the $Z/\gamma^\star$ cross section. Theoretical cross-sections normalised processes from the simulation. The $Z/\gamma^\star$ cross section was calculated up to next-to-next-to-leading-order (NNLO) in QCD including next-to-leading-order (NLO) electroweak corrections using FEWZ 3.1.b2 [48] configured with the MSTW2008NNLO parton distribution function (PDF) set.

The 2012 MC dijet samples JZXW, where X = 0 - 7, were used for the study of background. The samples were generated with PYTHIA 8. Table 5.1 shows the jet p_T range for each X

value of the JZXW samples.

Table 5.1: Lead jet p_T range for each X value of the JZXW samples.

JZXW	Jet p_T range [GeV]
JZ0W	0-20
JZ1W	20-80
JZ2W	80-200
JZ3W	200-500
JZ4W	500-1000
JZ5W	1000-1500
JZ6W	1500-2000
JZ7W	2000+

A detailed GEANT4 [49] model of the ATLAS detector and subdetector-specific digitisation algorithms was used to simulate the detector response for the MC sample.

5.2 Trigger Efficiency

The trigger efficiency was studied because while the event rates are reduced to a manageable size to be stored for offline analysis, it is important to maintain a signal efficiency which is as high as possible. A compromise must be made between reducing the event rate and signal efficiency. It is required that the tau trigger be able to distinguish between real tau leptons and signatures that may fake a tau lepton, such as from a jet or an electron. It is thus desired to have a high trigger efficiency for real taus, and a low trigger efficiency for background processes.

The trigger that was used in the baseline analysis was the tau125_medium1 (tau candidate $E_T > 125$ GeV, passing medium quality selection on the shower shape variables). This trigger was not ideal in the search for a heavy Z' resonance because the "medium" selection was applied online, but for the offline analysis, a "loose" selection was required. A "medium" selection corresponds to a higher signal purity than a "loose" one.
For this analysis the event selection criteria were:

- Leading tau and sub-leading tau have to pass the loose BDT ID
- Pass the tau125_medium1 trigger
- Lead tau $p_T > 150$ GeV
- Product of the tau charge equals -1

- Taus are back-to-back: $\phi > 2.7$ rad
- Transverse mass cut $m_T^{\text{tot}} > 850$ GeV. This cut allowed us to just focus on the mass points above 1.5 TeV due to the aim in improving the limit of 1.8 TeV found in Ref [43].

The new triggers of interest, which were run in 2012, were:

- The single jet trigger j360_a4tchad (jet with $E_T > 360$ GeV)
- The ditau trigger 2tau38T_medium1 (dijet with $E_T > 38$ GeV, passing medium selection)
- The specialised Z' trigger tau100_loose1_tau70_loose1 (tau candidate with $E_T > 100$ GeV or 70 GeV, passing loose selection)
- The combination tau100_loose1_tau70_loose1 or j360_a4tchad. This combination was chosen because both of these triggers perform well
- The combination tau125_medium1 or j360_a4tchad because tau125_medium1 peforms better at low p_T, while the other trigger performs better at higher p_T
- The combination tau125_medium1 or tau100_loose1_tau70_loose1 or j360_a4tchad. It was seen that the number of background events were reduced much more when the tau125_medium1 trigger was used compared to the other triggers. Both the tau100_loose1_tau70_loose1 and the j360_a4tchad trigger increased the number of signal events, with the effect being more noticeable when using the j360_a4tchad trigger.

The trigger tau100_loose1 is a specialised Z' decaying to hadronic taus trigger, and the j360_a4tchad trigger has a high efficiency at high p_T.

The trigger efficiency was defined as:

$$\text{Efficiency} = \frac{\text{N}_{\text{no trigger}}}{\text{N}_{\text{all cuts}}} \tag{5.1}$$

Where $\text{N}_{\text{no trigger}}$ = number of events passing all the requirements except the trigger, and $\text{N}_{\text{all cuts}}$ = number of events passing all the requirements.

Figure 5.2 shows the trigger efficiencies of the signal for the different triggers and their combinations for $m_{Z'} = 1875$ GeV, and Figure 5.3 shows trigger efficiencies for background

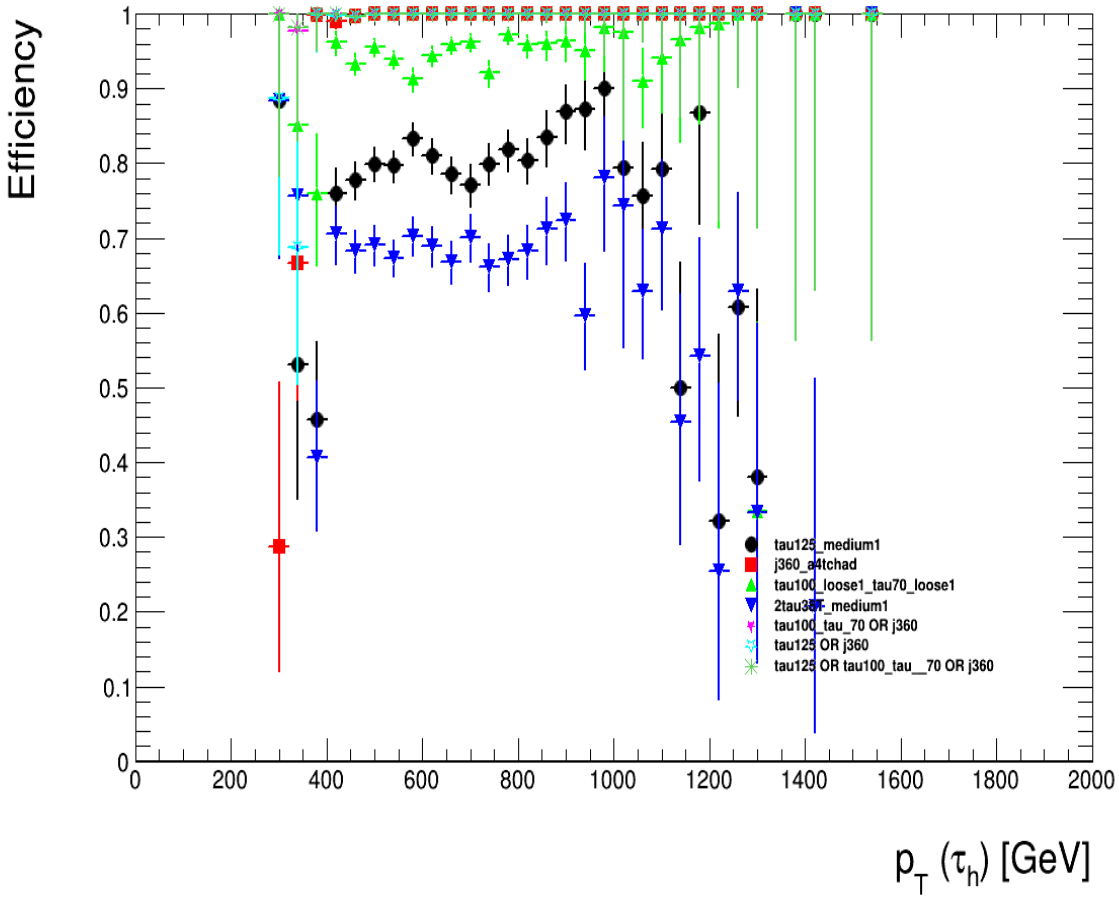

Figure 5.2: Trigger efficiencies for the Z' mass $m_{Z'} = 1875$ GeV.

processes, excluding multijets. The mass point $m_{Z'} = 1875$ GeV was chosen because this is the next mass point available, above the expected limit of 1.8 TeV [43].

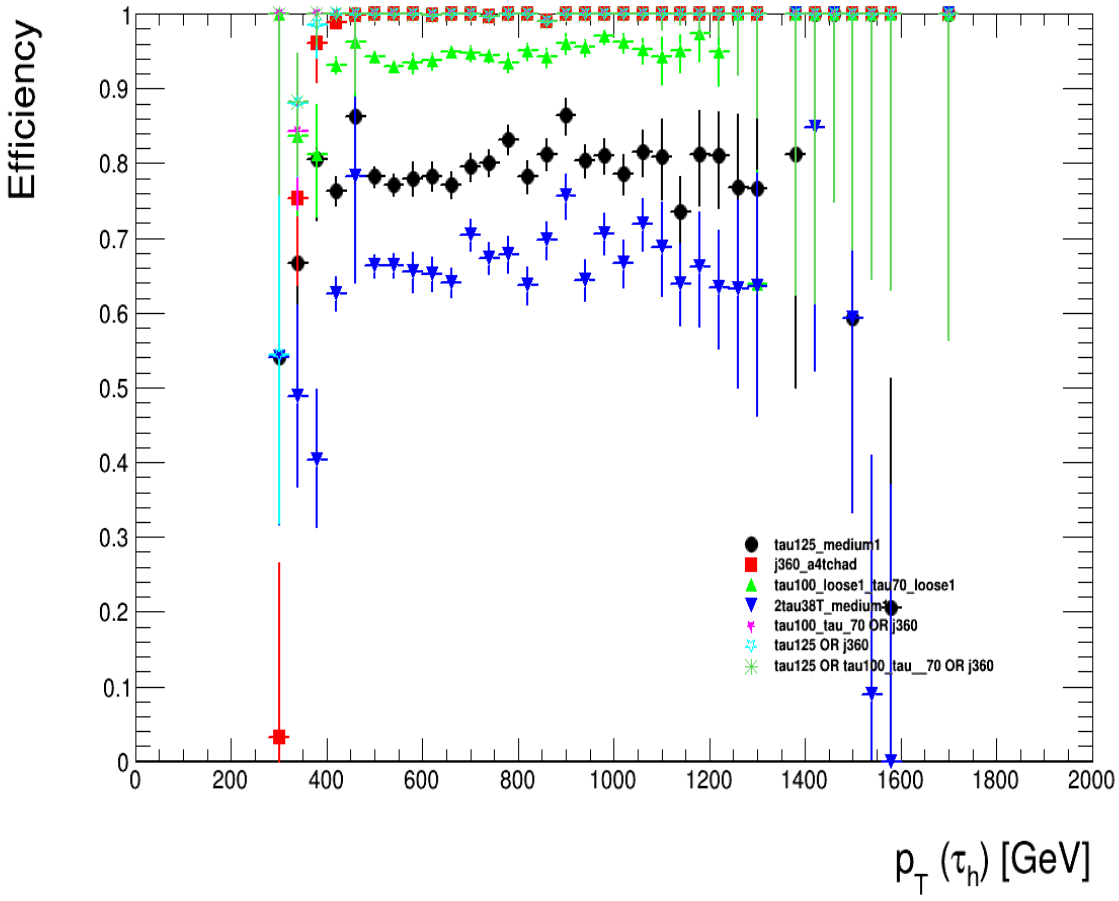

Figure 5.3: Trigger efficiencies for the background processes, not including multijets.

The significance values were calculated for the different triggers and their combinations using the formula:

$$\text{Significance} = \frac{\text{S}}{\sqrt{\text{B}}} \tag{5.2}$$

where S = number of signal events passing all the selection, and B = number of background events passing all the selection.

Table 5.2 shows the significance values of the triggers for the mass point 1875 GeV. The multijet background is excluded.

The j360_a4tchad trigger as well as combinations with it result in a high significance. Including this jet trigger boosts the signal efficiency by approximately 20%.

Table 5.2: Significance of the different triggers and their combinations for the mass point 1875 GeV.

Trigger	Significance
tau125_medium1	3.73
j360_a4tchad	4.20
tau100_loose1_tau70_loose1	4.09
2tau38T_medium1	3.44
tau100_tau70 OR j360	4.20
tau125 OR j360	4.20
tau125 OR tau100_tau70 OR j360	4.20

5.2.1 Improving Tau Identification using Tracking

For this part of the project, the case where taus are reconstructed as two-prongs in the nominal reconstruction and three-prongs in MC truth-seeded reconstruction (also known as pseudotracking), is studied. Truth-seeded tracking uses information from the MC simulated hits to reconstruct the tracks, thus bypassing the pattern recognition. This represents an "ideal" tracking scenario. The pseudotracking technique was used because it allowed for the identification and categorisation of taus to investigate their properties, as well as of the tracks, in the nominal reconstruction. The nominal reconstruction is the standard reconstruction used throughout ATLAS. This process uses the stored raw data, and specific reconstruction algorithms for purposes such as particle identification, E_T^{miss} determinaion, and primary vertex determination. Pattern recognition algorithms are used to search for the tracks [50]. The wrong number of tracks may be reconstructed in the nominal reconstruction due to the tracking's inefficiency to correctly split hits, or allow tracks to share hits.

The process to study track merging in a high-density environment began with investigating the comparison between two cases: the case with two-prong taus in the nominal reconstruction and three-prong taus in pseudotracking, and the case where the taus are reconstructed as three-prongs in both the reconstruction and the pseudotracking. The former case is defined as the "migrated" taus case and the latter the "good" taus case.

Custom produced ntuples of Drell-Yan $Z/\gamma^\star \to \tau\tau$ samples were produced which contain track variables and pseudotrack variables to provide full and detailed information about the tracking. For the analysis it was important to match tracks to their corresponding pseudotracks to ensure a direct comparison between them. The tracks were associated by matching their MC barcode, which is a unique identifier for every truth particle in the MC event. Throughout this investigation, $Z/\gamma^\star \to \tau\tau$ sample with the mass range 1750 GeV $<$ $M_{\tau\tau}$ $<$ 2000 GeV was used, to provide a source of high p_T tau leptons for investigation.

Tracks in "migrated" taus were classified by identifying each pseudotrack as either "lost",

"closest", or "other" track. The "lost" track was defined as the pseudotrack that was not matched to its corresponding reconstructed track, and the "closest" track was defined as the track with smallest ΔR between the "lost" track and the track investigated. The "other" track is thus the third track. The reconstructed tracks were then matched to the "closest" and the "other" track, producing the two-prongs in nominal reconstruction.

A set of common pre-selection criteria were applied in the beginning of the analysis to the tau candidates. These were:

- Transverse momentum of tau candidate $p_T > 50$ GeV
- $|\eta| < 2.47$ excluding the crack region, $1.37 < |\eta| < 1.52$
- Pass loose BDT (Boosted Decision Tree) ID. The BDT technique discriminates hadronic tau decays against jets, and the "loose" requirement gives a high signal efficiency.

Results

Various variables were used to compare the tau properties between the "migrated" taus and the "good" taus case. Looking at the τ p_T variable in Figure 5.4, it was confirmed that "migrated" taus typically have higher p_T than "good" taus, as expected, since higher p_T taus are more likely to suffer from track loss issues, since the tracks are more highly collimated.

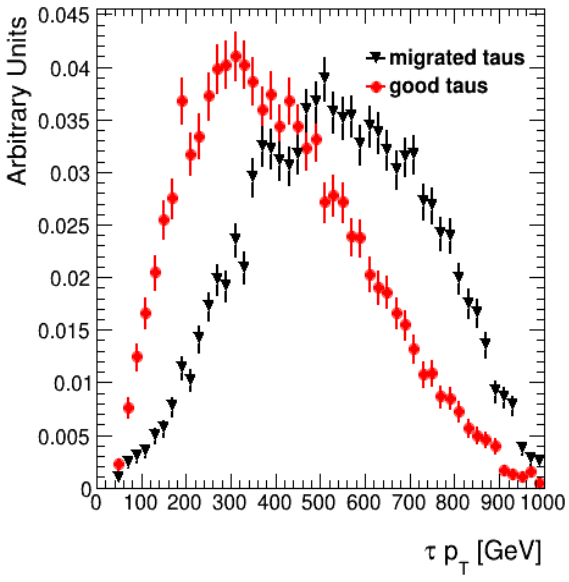

Figure 5.4: The distribution of the "migrated" taus typically peak at a larger p_T than the "good" taus.

Other variables studied were the mass balance variable defined as:

$$\frac{m_\tau^{\text{track}} - m_\tau^{\text{calo}}}{m_\tau^{\text{track}}} \tag{5.3}$$

where m_τ^{track} is mass of the tau candidate calculated from the tracks, and m_τ^{calo} is the invariant mass using the energy deposit in the calorimeter which is associated to the tau. Figure 5.5 shows this variable. Since for the "migrated" taus case the taus have lost a track, the values of the m_τ^{track} variable will be much lower than the values for the m_τ^{calo} variable. From the definition of the mass balance it is reasonable that the "good" taus case would have a peak closer to 0.

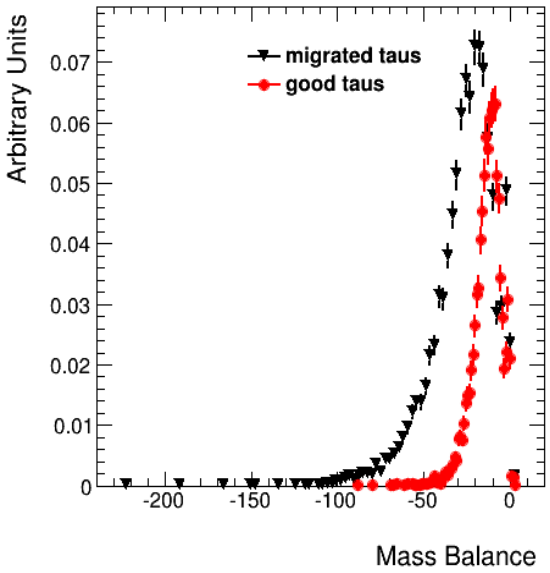

Figure 5.5: A comparison between the "good" taus and the "migrated" taus for the mass balance variable. The "good" taus case has a peak closer to 0.

Figure 5.6 shows the variable $\frac{E_T^\tau}{p_T^{\text{total}}}$ which is defined as:

$$\frac{E_T^\tau}{p_T^{\text{total}}} = \frac{\sum E_T^{\text{cluster}}}{\sum p_T^{\text{track}}} \tag{5.4}$$

This variable thus shows the E_T of the tau cluster divided by the sum of the track p_T.

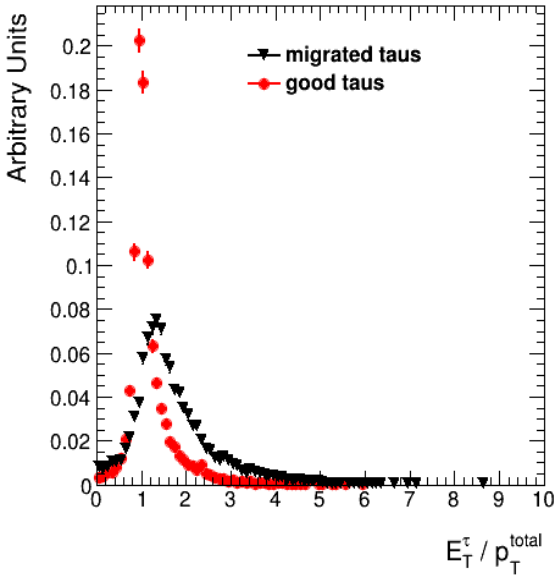

Figure 5.6: The ratio of the τ E_T over the sum of the track p_T is considered.

Figure 5.7 shows the corrected energy where the E_T of the neutral pion cluster has been subtracted from the E_T of the tau cluster, and divided by the sum of the track p_T. This variable is defined as:

$$\frac{E_T^{\text{corrected}}}{p_T^{\text{total}}} = \frac{\sum E_T^{\text{cluster}} - \sum E_T^{\text{neutrals}}}{\sum p_T^{\text{track}}}. \tag{5.5}$$

The total E_T of the tau cluster includes that of the charged and neutral pions, thus by excluding the effect from the neutral pions the focus can be just on charged pions, which are the particles of interest.

Figure 5.7 shows that the "good" taus peak at approximately 1 because all the three charged tracks that characterise tau decays are present, and thus the ratio of tau E_T over the sum of the track p_T would be almost one-to-one. This is the same as for the ratio of the corrected energy and the sum of track p_T. Since the "migrated" taus have lost a track, the ratio would be larger than 1 because the sum of the track p_T would have decreased.

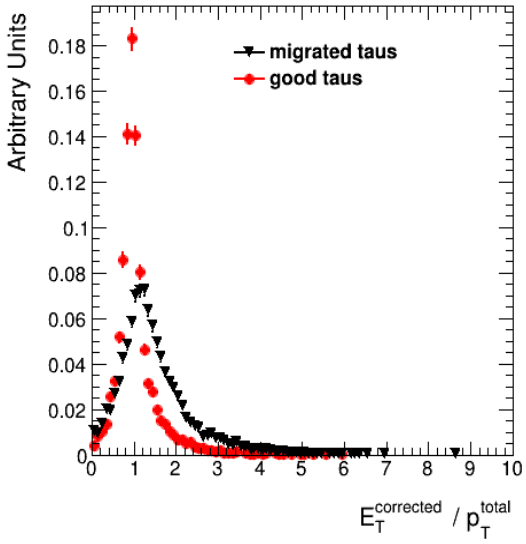

Figure 5.7: The ratio of the τ cluster E_T, which excludes the energy of the neutral pion cluster, over the sum of the track p_T is considered.

Another variable that was investigated was the track spread W^{τ}_{track} shown in Figure 5.8. This is defined as:

$$W^{\tau}_{\text{track}} = \frac{\sum (\Delta R^{\text{track}})^2 \cdot p_T^{\text{track}}}{\sum p_T^{\text{track}}} - \frac{(\sum \Delta R^{\text{track}} \cdot p_T^{\text{track}})^2}{(\sum p_T^{\text{track}})^2}. \tag{5.6}$$

The track spread shows the spread of tracks in η, ϕ space, relative to their p_T. This variable thus relates the distance of the track to the tau candidate (ΔR^{track}) with the track p_T.

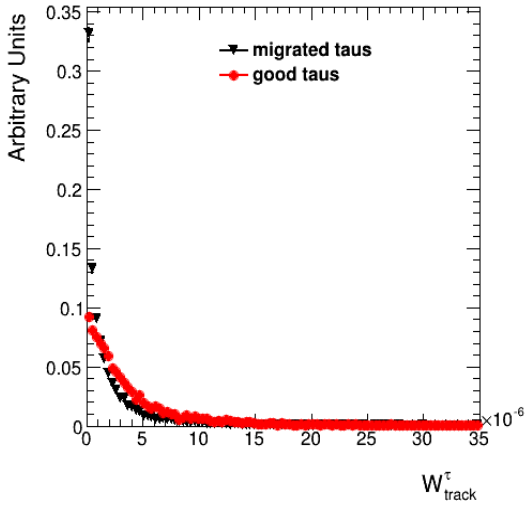

Figure 5.8: The track spread variable relates the spread of the tracks with the p_T of the tracks. The "good" taus case and the "migrated" taus case are compared.

So far, cut-based variables have been investigated to compare tau properties between the "migrated" taus and the "good" taus. Some differences are noticeable from the plots.

Identifying hadronically decaying tau leptons will be met with the difficulty of trying to distinguish them from hadronic jets that are produced in various physics processes, such as multijet production. Other background contributions come from W+jets, Z+jets, $t\bar{t}$, single top quark, and diboson production [43, 51]. It is thus an objective in this two-prong tau recovery study that the two-track jet background is differentiated between the two-track taus. For this investigation, the 2012 data sample was filtered to contain two-track objects which could be identified as jets but with tau-like properties. In order to obtain a sample of events which did not contain any real taus, events were required to:

- Pass a single jet trigger
- Electron and muon veto (removing electrons and muons from the events)
- No "good" taus (not reconstructed as one or three-prongs and do not pass the loose BDT ID)
- Pass the back to back requirement where $\cos\Delta\phi <$ -0.95.

In addition to the above selections, a dijet 'tag and probe' method was used. This technique is a data driven one and it allows for the efficiency of the probe passing a selection criteria to be determined. For this study, two tau candidates are chosen back-to-back and with a loose p_T requirement. One tau candidate is the tag and the other is the probe. The selections for the tag aim to increase the dijet purity while keeping the events with real taus low, and the probe should be unbiased. Since loose BDT ID was applied in the analysis, the probe was also required to pass the loose BDT ID. The probe is thus a jet with tau-like properties, and is used as a control sample of fake taus for the study. Table 5.3 shows the respective selections.

Table 5.3: Tag and probe dijet selections.

Tag	Probe
$p_T > 50$ GeV	$p_T > 50$ GeV
$\lvert\eta\rvert < 2.47$, $1.37 < \lvert\eta\rvert < 1.52$	$\lvert\eta\rvert < 2.47$, $1.37 < \lvert\eta\rvert < 1.52$
Not pass loose BDT ID	Pass loose BDT ID
Number of τ tracks ≥ 4	Number of τ tracks $= 2$

With the hopes of reducing the two-track jet background, a method was developed that compared the cut-based variables so that the ones with the best discrimination power against

the multijet background could be identified. The variables described in the beginning of Section 5.2.1 were studied.

Figure 5.9 and Figure 5.10 show the tau variable distributions and track variable distributions, respectively, for the 'tag and probe' approach. Some of the shape of the distributions shown in Figure 5.9 and Figure 5.10 for the "migrated" taus are very similar to those of the probe tau candidates. The reason for their similarity is that by requiring the probe to pass loose BDT ID, tau-like jets are selected and jets also suffer from track merging at high p_T. Figure 5.9 a) shows, however, a significant difference in the distributions of the "migrated" taus and the probe tau candidates. The "migrated" taus have large transverse momenta because it is at high p_T that track merging occurs, but the probe tau candidates are jets, and jets typically have lower p_T than the $Z' \rightarrow \tau_{had}\tau_{had}$ events. MC dijet sample skims were produced. In addition to comparing the "migrated" taus in MC with the probe tau candidates in data, the "two-prong" taus case were also compared to tau candidates that passed the probe selection in the MC dijet sample. In the "two-prong" taus case, the taus are reconstructed as two-prongs in both the pseudotracking and the nominal reconstruction. These did not arise from the track merging problem but are usually due to one-prong taus picking up an extra track from conversions of neutral pions.

For the tau candidates in the dijet sample, JZ7W sample (lead jet $p_T > 2$ TeV) was used. At this energy, a source of high p_T jets were produced. The probe tau candidates in data show similar behaviour to tau candidates in the dijet sample, as seen in Figure 5.11.

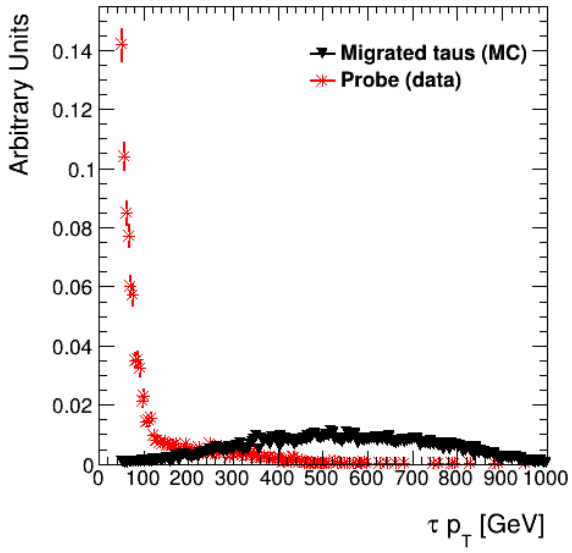

a)

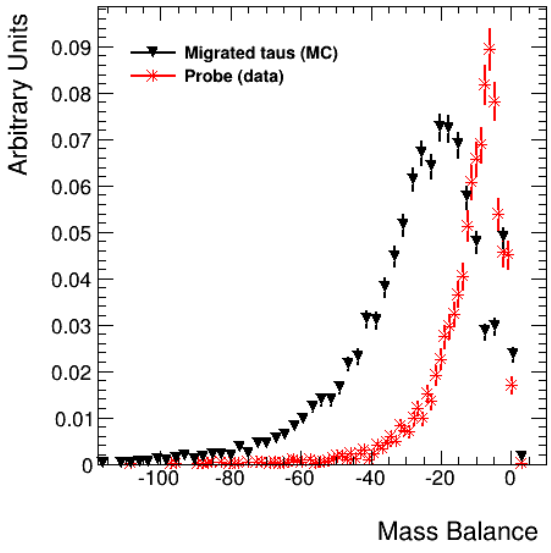

b)

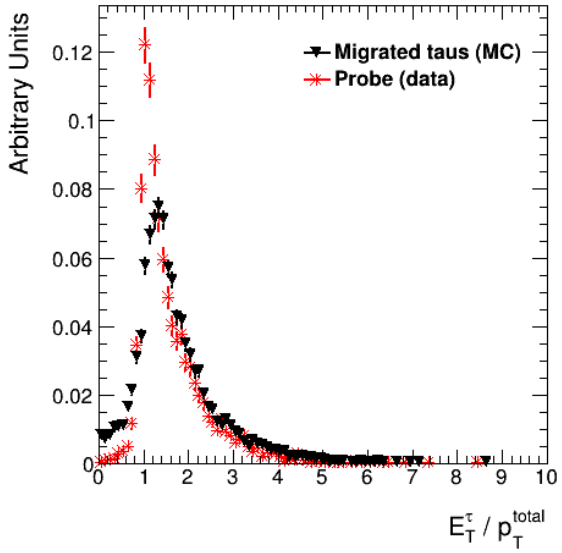

c)

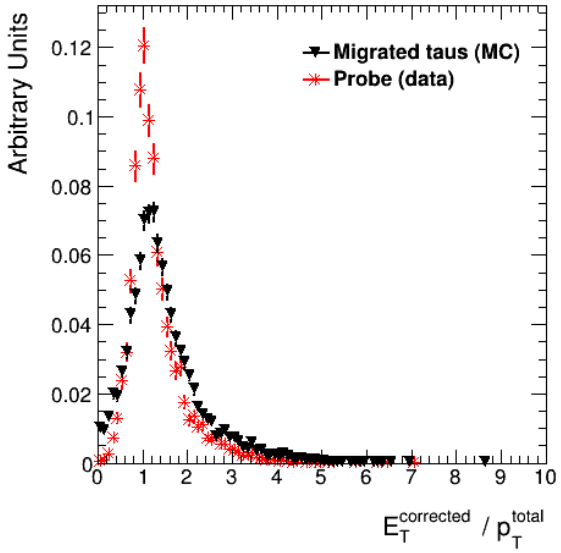

d)

Figure 5.9: Tau variables were investigated. The "migrated" taus in the $Z/\gamma^{\star} \rightarrow \tau\tau$ sample was compared with the probe tau candidates in data.

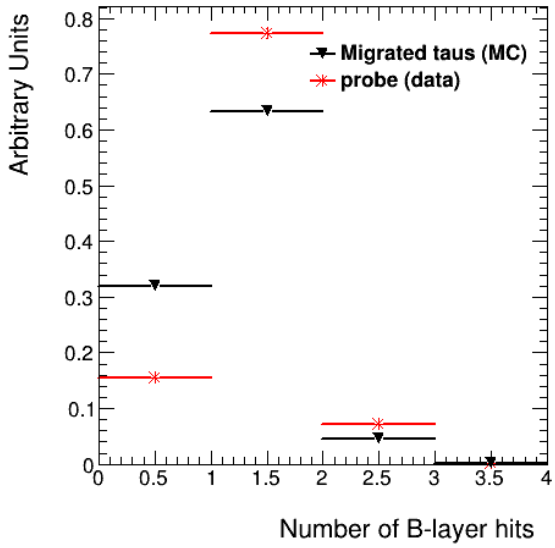

a)

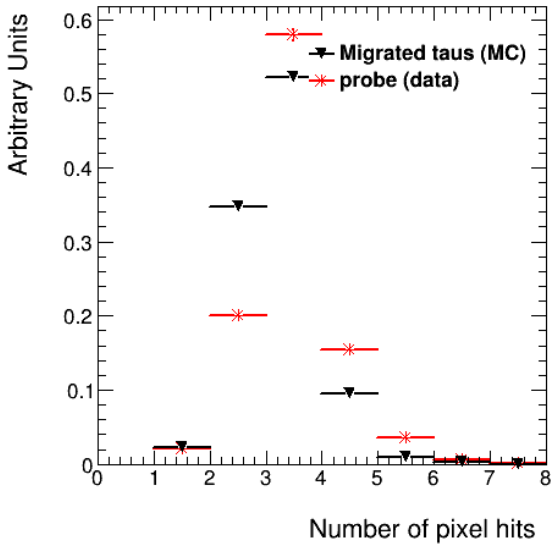

b)

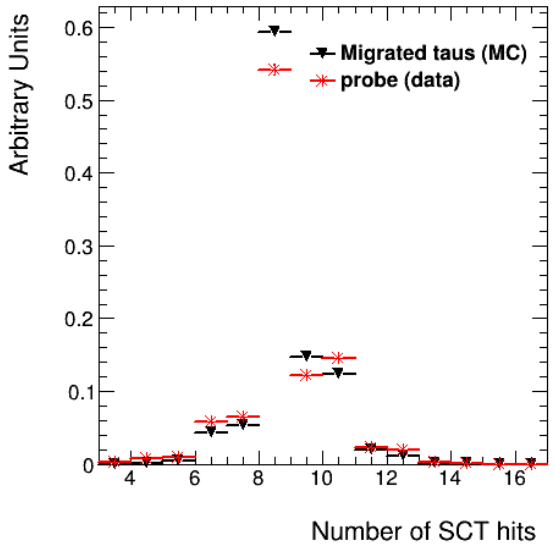

c)

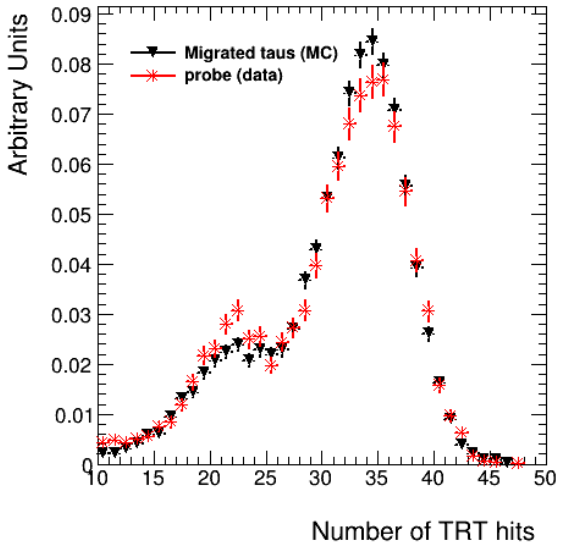

d)

Figure 5.10: These track variables investigated show the number of hits in the various regions of the inner detector.

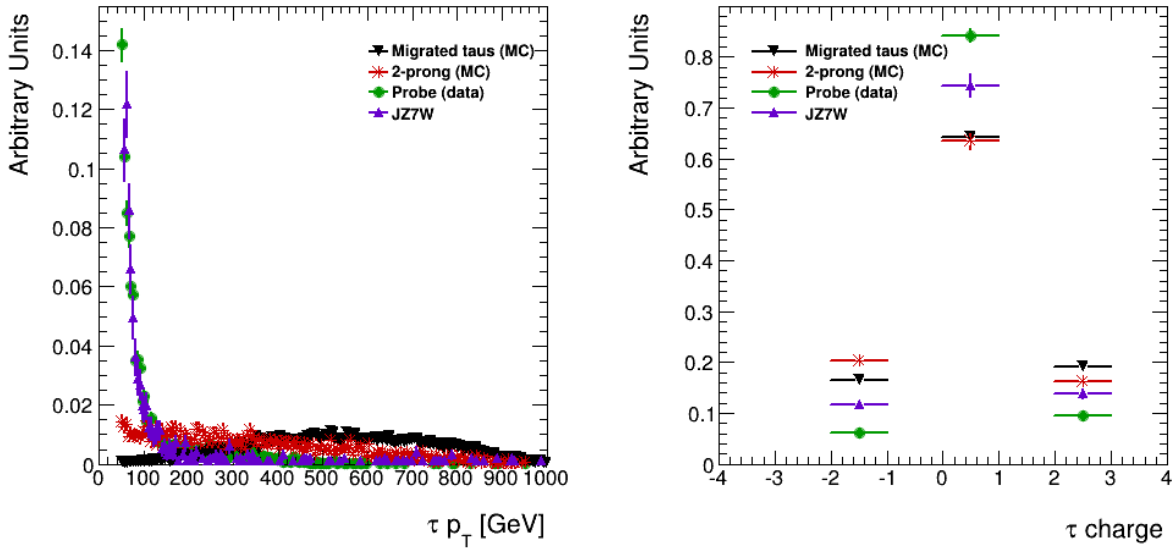

a) b)

Figure 5.11: Plot a) shows the τ p_T distribution and plot b) shows the τ charge distribution. These plots compare together the "migrated" taus in $Z/\gamma^\star \to \tau\tau$ sample, "two-prong" taus in $Z/\gamma^\star \to \tau\tau$ sample, probe tau candidates in data, and tau candidates in the dijet JZ7W sample.

The efficiency of recovering the τ charge was also determined. Table 5.4 contains the efficiency for the number of tau candidates passing the criteria that charge equals 2 for four cases. The choice for this criteria is due to the fact that real taus should have charge $= \pm 1$, and a tau is reconstructed from one or three charged tracks. Because of this it would be possible to deduce the charge of the lost track for the "migrated" taus case by requiring that absolute charge equals 2 since the sum of the charge of the three tracks need to be ± 1. Then, with information from all the tracks, the charge of the tau can be recovered. From Table 5.4 it is seen that the tau charge can be recovered for about 35% of the "migrated" taus. The efficiency was determined by calculating the ratio of the number of tau candidates passing the criteria divided by the total number of tau candidates in each case.

Table 5.4: Efficiency in % for tau candidates to have absolute charge equal to 2.

Criteria	Migrated taus (MC)	2-prong taus (MC)	Probe taus (data)	JZ7W (MC)
$\|\text{charge}\| = 2$	35.7	36.6	15.7	25.6

Other tau variables were investigated, as shown in Figure 5.12.

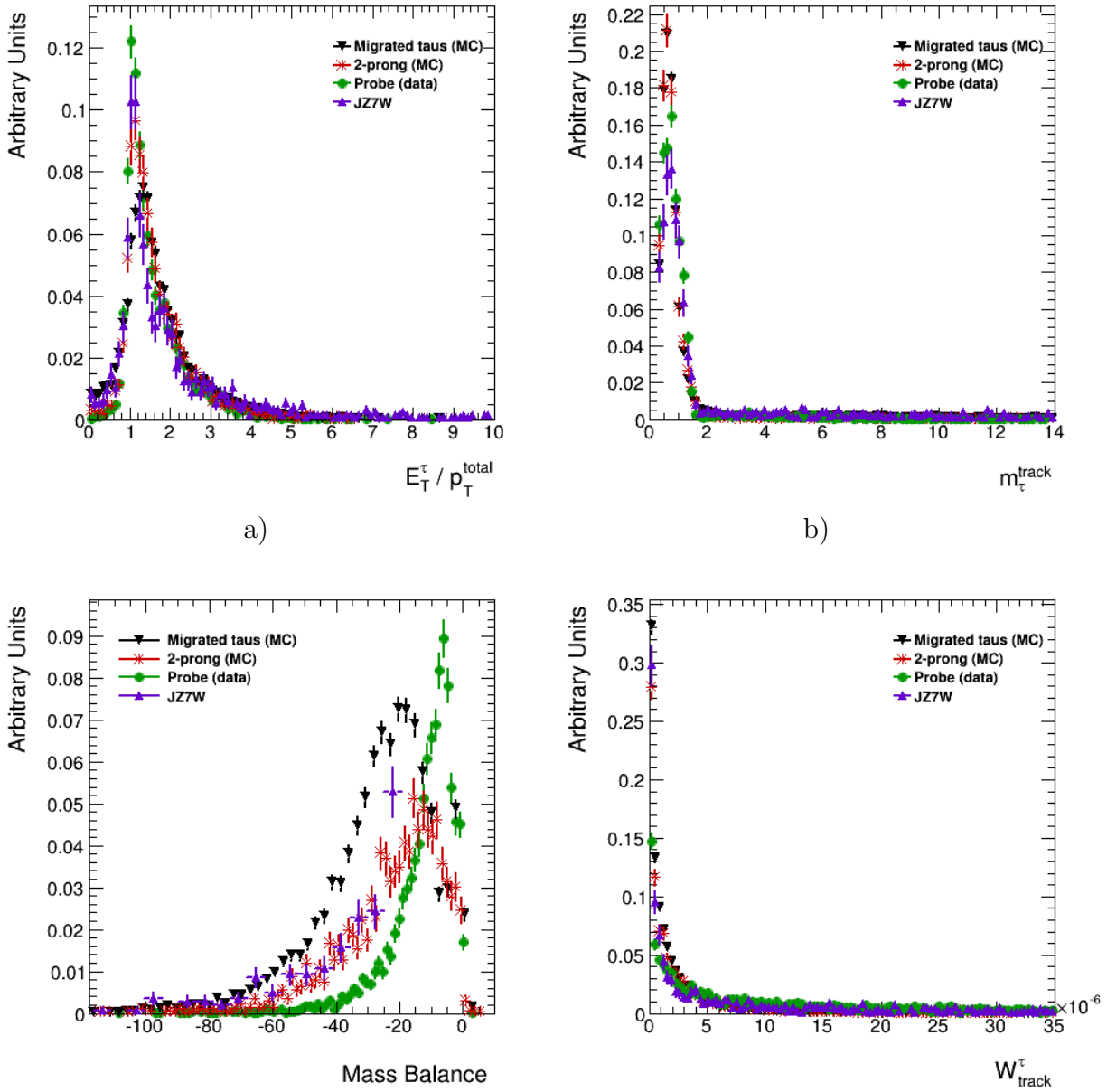

Figure 5.12: Tau variable distributions for the "migrated" taus in $Z/\gamma^\star \to \tau\tau$ sample, "two-prong" taus in $Z/\gamma^\star \to \tau\tau$ sample, probe tau candidates in data, and tau candidates in the dijet JZ7W sample. Figure a) compares the $\frac{E_T^\tau}{p_T^{\text{total}}}$ variable for the four cases, Figure b) compares the m_τ^{track} variable, Figure c) compares the mass balance variable, and Figure d) compares the track spread.

Track variables were also studied as shown in Figure 5.13 and Figure 5.14. Figure 5.14 shows the combination of the number of shared pixel hits and the number of split pixel hits variables.

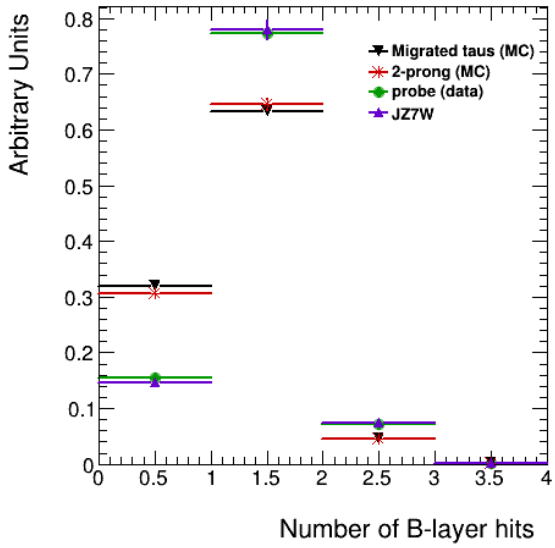

a)

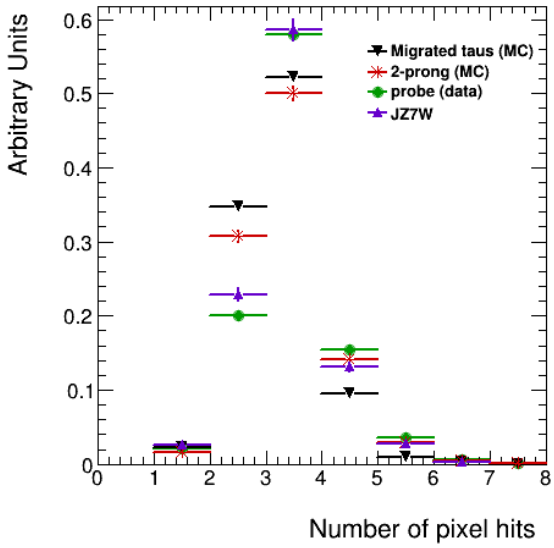

b)

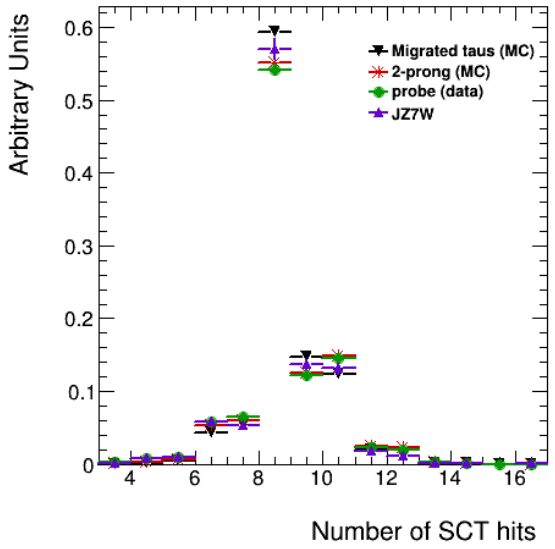

c)

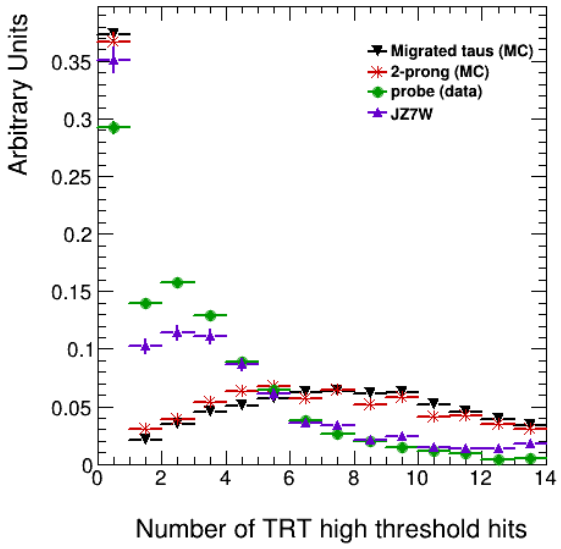

d)

Figure 5.13: Track variable distributions for the "migrated" taus in $Z/\gamma^{\star} \rightarrow \tau\tau$ sample, "two-prong" taus in $Z/\gamma^{\star} \rightarrow \tau\tau$ sample, probe tau candidates in data, and tau candidates in the dijet JZ7W sample. Figure a) compares the number of B-layer hits, Figure b) compares the number of pixel hits, Figure c) compares the number of SCT hits, Figure d) compares the number of TRT high threshold hits

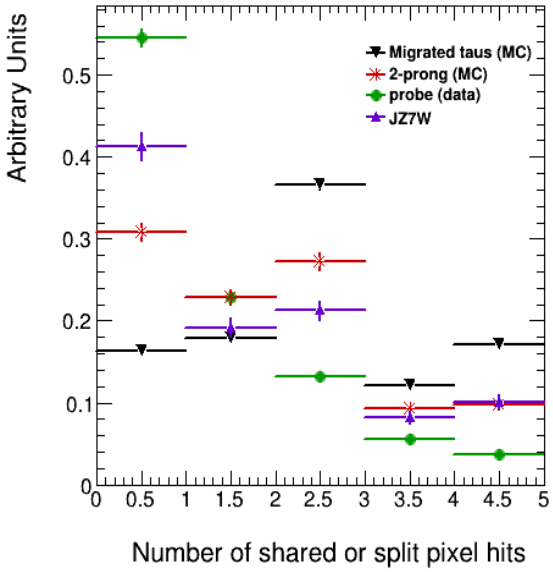

Figure 5.14: This variable is the result of combining the number of shared pixel hits and the number of split pixel hits variables.

The tau and track variables that were investigated have some discrimination power against the two-track jet background. The tau BDT jet score was also considered, as shown in Figure 5.15. This variable provides the best separation power out of all the variables considered.

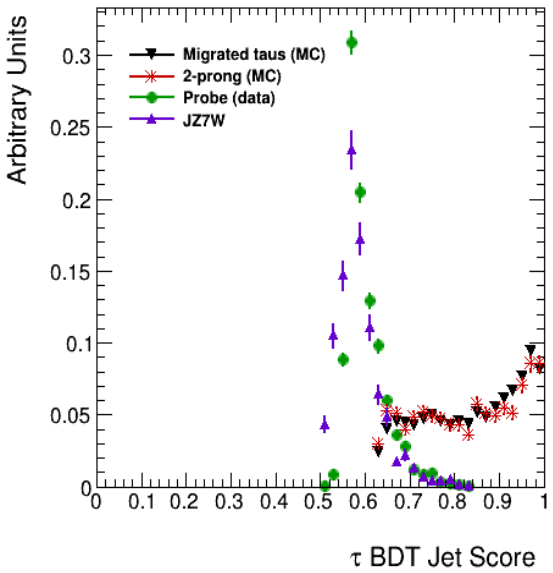

Figure 5.15: The BDT jet score shows a high discrimination power against the background.

The BDT jet score is an indication of how tau-like an object is. The higher the score, the tighter the tau ID. It looks promising from Figure 5.15 that allowing the two-prong taus to

pass medium ID a large number of the background can be removed. Various requirements on the BDT jet score were also applied and investigated. Table 5.5 shows the efficiencies for the number of tau candidates passing medium BDT ID and certain requirements on the BDT jet score.

Table 5.5: Efficiency in % to pass various requirements on tau BDT output.

Criteria	Migrated taus (MC)	2-prong taus (MC)	Probe taus (data)	JZ7W (MC)
Pass medium BDT ID	90.0	87.6	47.4	42.7
BDT > 0.60	100.0	100.0	38.9	29.8
BDT > 0.65	95.7	94.6	12.6	9.6
BDT > 0.70	84.9	82.7	3.7	3.5
BDT > 0.75	73.4	70.2	1.0	1.4
BDT > 0.80	62.5	58.7	0.1	0.2

A large fraction of the jet background can be rejected by applying requirements on the BDT score while keeping the signal efficiency high. If the BDT > 0.65 criteria was considered, from Table 5.5 it can be seen that about 90% of jet fakes can be rejected while keeping a high signal efficiency of about 95%. It must be noted though that the BDT threshold is p_T dependent, and applying requirements on them may affect scale factors which are used to correct the MC modelling. This would cause a problem because these scale factors are provided by the Tau Working Group, and deviating from them would require approval from the group. Another approach was investigated in parallel to this BDT score study, using a "point score" method. This method was applied to those variables in Figure 5.12 and Figure 5.13 because they have some discriminating power, but are not very effective when considered alone. The "point score" method works by assigning a point of 1 to every tau candidate that passes a criteria that has been set on various variables, and real two-prong taus should have a higher score than the two-track jets. Table 5.6 shows the variables and the criteria used for this method.

The thresholds on the set of criteria in Table 5.6 were chosen only by eye, thus there is further scope for optimisation. The resultant "point score" distribution is shown in Figure 5.16.

Table 5.6: Variables and criteria for the "point score" method. Tau candidates are assigned a point for each criteria they meet.

Variable	Criteria
Number of TRT high threshold hits	≥ 4
Number of shared or split pixel hits	> 0.0
W^{τ}_{track}	$< 1\text{x}10^{-6}$
W^{τ}_{track}	$< 5\text{x}10^{-6}$
$m_{\tau}^{\text{track}}/1000.0$	< 2.0
Mass balance	$<$ -15.0
BDT Jet Score	> 0.65
BDT Jet Score	> 0.75
τ charge	$= 2$

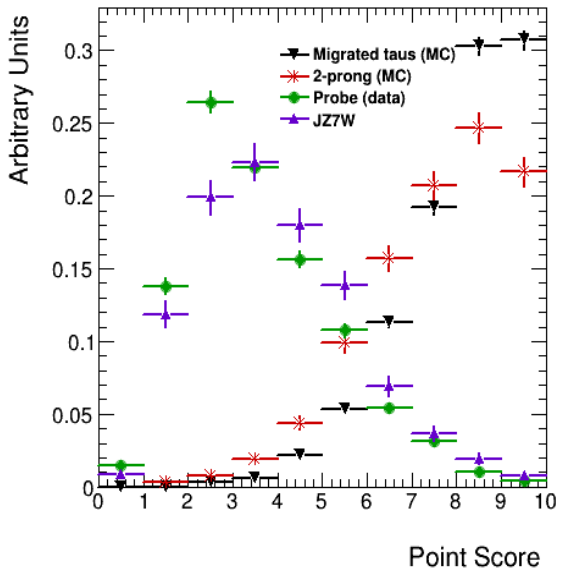

Figure 5.16: The "point-score" plot shows that, on average, the two-prong taus have a higher score than the jet background.

Table 5.7: Efficiency in % to pass "point score" thresholds.

Criteria	Migrated taus (MC)	2-prong taus (MC)	Probe taus (data)	JZ7W (MC)
point score ≥ 4	99.2	97.5	36.4	45.4
point score ≥ 5	97.5	93.6	20.7	27.5

The efficiency of the tau candidates passing requirements applied to the "point score" was also calculated. Their values are shown in Table 5.7.

The "point score" method shows promise in being a variable with good discriminating power against the jet background, but the cut thresholds could benefit from further optimisation. Even better performance could be achieved by combining the variables in a BDT or Neural

Network (NN) so that correlations are taken into account, but this is beyond the scope of this study. NN is an algorithm that is able to perform pattern recognition effectively, thus it is useful in resolving shared hits in a dense environment in the detector [52].

An attempt was also made to assign a charge to the tau. The approach was to compare the sign of the charge of the lost pseudotrack to the sign of the charges of the two found tracks in the nominal reconstruction, and define the two found tracks as same sign (SS) and opposite sign (OS) depending on their charge with respect to the charge of the lost pseudotrack.

For this study, only a subset of taus reconstructed as charge equal to 0 were investigated. Since real taus have charge = $\pm$ 1, charge equal to 0 would indicate that the charge of its track components are opposite in sign. However, with this requirement alone, it would not be possible to deduce the sign of the charge of the lost pseudotrack. To obtain more information, the track with the same sign (SS) and opposite sign (OS) to the lost pseudotrack was compared. This was an attempt to identify various properties of the two tracks that could point to it as having the same sign charge or opposite sign charge to the lost track.

Figure 5.17 and Figure 5.18 show the comparison between the distribution for the SS and OS tracks to the lost pseudotrack. Very little discrimination between the SS and OS tracks is observed.

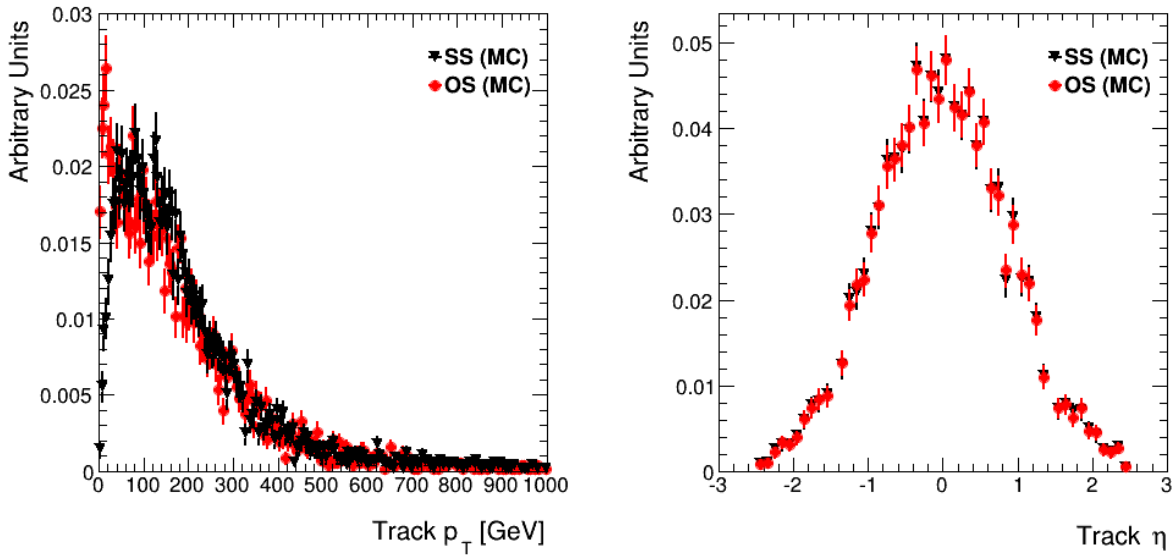

a) b)

Figure 5.17: These track variable plots compare the distributions between the SS and OS tracks in the $Z/\gamma^{\star} \rightarrow \tau\tau$ sample.

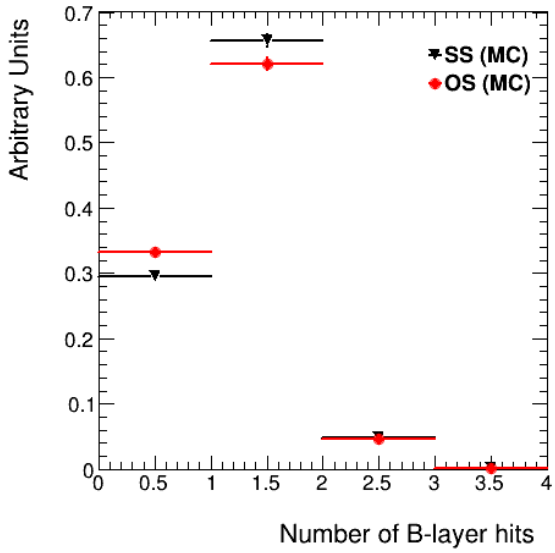

a)

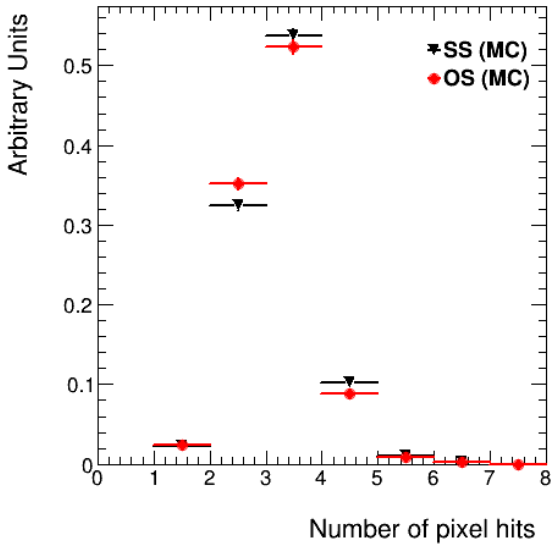

b)

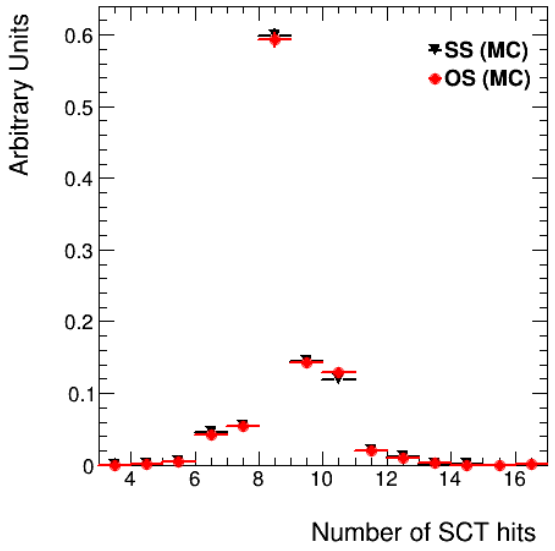

c)

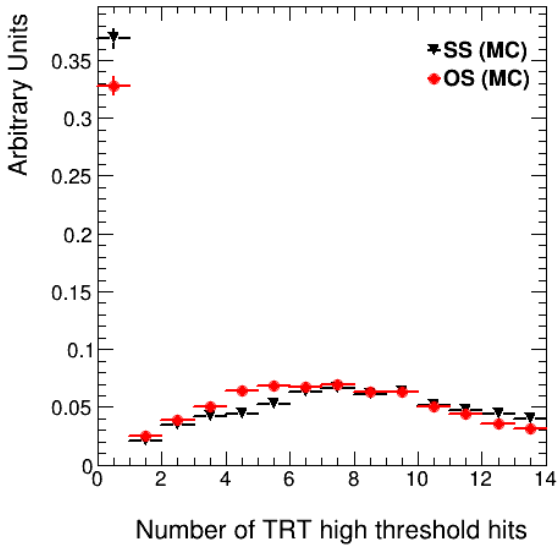

d)

Figure 5.18: These plots compare the number of hits distributions between the SS and OS tracks in the $Z/\gamma^{\star} \rightarrow \tau\tau$ sample.

Chapter 6

Summary

In an attempt to increase the sensitivity of the search for the Z' boson decaying to hadronic tau pairs in the Sequential Standard Model, an investigation was made into the improvement of the trigger efficiency and the tau identification using tracking. The 2012 data sample was used and it was recorded by the ATLAS detector in proton-proton collisions at $\sqrt{s} = 8$ TeV, and had an integrated luminosity of 19.5 fb^{-1}.

Triggers are optimised to have higher signal efficiency and lower background efficiency to ensure a focus on the events of interest, and also the fact that too many events are produced and currently it is not possible to store all the data. For the study, several new triggers, such as the jet trigger EF_j360_a4tchad (Event Filter jet $E_T > 360$ GeV) and a specialised Z' trigger, as well as combinations of them were studied for $m_{Z'} = 1875$ GeV. Their significance values were calculated with the Poisson significance, and it was shown that the EF_j360_a4tchad trigger had the highest significance value. Including it boosted the $Z' \to \tau\tau \to \tau_h\tau_h + 2\nu_\tau$ signal by about 20%.

In this analysis there are many background processes, such as multijets, that may fake the signature of a tau in the detector. Hadronic taus can be classified into one-prong decay with one charged track or three-prong decay with three charged tracks, but at high p_T the taus may be reconstructed as two-prongs instead of as three-prongs. This is the result of track merging, and it decreases the sensitivity of the analysis. In this study, the taus that were reconstructed with the wrong number of tracks were called the "migrated" taus. Various cut-based variables were investigated to compare the tau properties between the "migrated" taus with the taus in an ideal case where track merging was not a problem. The study also included investigating variables that could exhibit good discrimination power against the two-track jet background. The 'tag and probe' method was used and from this approach it was determined that the tau BDT jet score was a promising variable. However, its working point thresholds are p_T dependent. Requirements were applied to it and about 90% of jet fakes could be rejected while keeping a high signal efficiency of about 95%. However,

applying requirements on the BDT jet score alters scale factor values which are set by the Tau Working group. Deviating from those values would need the agreement of the group. The "point-score" method was also of interest, and room for its optimisation is possible. For each tau candidate that passed a certain criteria a point was assigned to it. This produced comparable performance with the case of applying requirements to the BDT jet score.

It was also attempted to assign a charge to the tau. The same sign (SS) and opposite sign (OS) plots were compared to find properties that could indicate the sign of the charge of the tracks. However, the distributions were very similar and it is not possible to deduce the sign of the charge of the tracks relative to the lost track using this information alone.

In the future, it may be possible to modify the tracking reconstruction algorithms so that this information can be determined, and using lower level hit variables which were not available in the ntuples. Different techniques and ideas for improving the sensitivity of the Z' analysis were investigated, and have provided useful input to the Tau and Tracking performance groups as ideas for future performance improvements.

Not only are effective reconstruction algorithms crucial for the identification of particles, but so too is the effective performance of detector components. This dissertation looked at the ATLAS hadronic Tile Calorimeter which contributes to the identification of particles and jets because it provides accurate measurements of energy and position of objects in the detector. In order to have a good energy resolution of these objects, it is required to have uniform light distribution in the scintillation counters. Thus, this dissertation showed the preliminary study of the light collection uniformity and response of the crack scintillation counters of the ATLAS hadronic Tile Calorimeter, as part of the contribution to the ATLAS upgrade.

The scintillation counters have a sheet of aluminium covering, and measurements were recorded for the case with counters with the aluminium cover and repeated for the case without the cover. The response non-uniformity, calculated by dividing the root mean square value (rms) by the mean, for the case without the cover was about 1% less than if the cover was in place. However, the covering was required to protect the counters from mechanical damage. It was observed that many factors were considered in order to increase the light yield. This included wrapping Tyvek paper around the counters so that the probability of internal reflection increased, and aluminizing those ends of the wavelength shifting fibers that were away from the photomultiplier tubes. However, many factors also decreased the light collection uniformity. This included the arrangement of the wavelength shifting fibers, having tapes around the fibers which were used to secure them in place, or having the aluminium tapes which held the cover together. The intensity of the light decreased exponentially as it travelled through the scintillation counters. There is still much to be

investigated on the cause of the features seen, but this preliminary study emphasised the importance of the detector upgrade to have optimum performance of the components.

Bibliography

[1] ATLAS Collaboration, *The ATLAS Experiment at the CERN Large Hadron Collider*, JINST 3 S08003 (2008).

[2] CMS Collaboration, *The CMS experiment at the CERN LHC*, JINST 3 S08004 (2008).

[3] ALICE Collaboration, *The ALICE experiment at the CERN LHC*, JINST 3 S08002 (2008).

[4] LHCb Collaboration, *The LHCb Detector at the LHC*, JINST 3 S08005 (2008).

[5] Tara Shears, *The Standard Model*, Phil. Trans. R.Soc. A (2012) 370, 805817.

[6] J. Beringer et al. *Particle Data Group*, Phys. Rev. D86, 010001 (2012).

[7] Gninenko, S.N. et al., *Invisible Z-prime as a probe of extra dimensions at the CERN LHC*, Phys.Rev. D78 (2008) 097701.

[8] ATLAS Collaboration, *Expected Performance of the ATLAS Experiment, Detector, Trigger and Physics*, CERN-OPEN-2008-020, Geneva, 2008.

[9] A. Kaczmarska, J. Piatlicki, T. Przedzinski, E. Richter-Was, Z. Was. *Application of TauSpinner for studies on tau-lepton polarization and spin correlations in Z, W and H decays at LHC*, arXiv:1402.2068, 2014.

[10] K. R. Lynch et al, Phys. Rev. D 63, 035006 (2001).

[11] ATLAS Collaboration, *Identification of the Hadronic Decays of Tau Leptons in 2012 Data with the ATLAS Detector*, ATLAS-CONF-2013-064, 2013.

[12] ATLAS Collaboration, *Measurement of Jet Mass and Substructure for Inclusive Jets in $\sqrt{s}$ = 7 TeV pp Collisions with the ATLAS Experiment*, ATLAS-CONF-2011-073, 2011.

[13] ATLAS Collaboration, *Studies of the impact and mitigation of pile-up on large radius and groomed jets in ATLAS at $\sqrt{s}$ = 7 TeV*, ATLAS-CONF-2012-066, 2012.

[14] Dr. Dave Goldberg. *Where does the Standard Model of physics come from?*. [Accessed: 12/03/2014]; Available from: http://io9.com/where-does-the-standard-model-of-physics-come-from-599641558.

[15] David J. Griffiths, 1987. *Introduction to Elementary Particles*, New York: John Wiley & Sons, Inc.

[16] P.W. Higgs, Phys. Rev. Lett. 13, 508 (1964); Phys. Rev. 145, 1156 (1966); F. Englert and R. Brout, Phys. Rev. Lett. 13, 321 (1964); G.S. Guralnik, C.R. Hagen, and T.W. Kibble, Phys. Rev. Lett. 13, 585 (1964).

[17] ATLAS Collaboration, *Observation of a new particle in the search for the Standard Model Higgs boson with the ATLAS detector at the LHC*, Phys. Lett. B 716 (2012) 129, arXiv:1207.7214 [hep-ex].

[18] CMS Collaboration, *Observation of a new boson at a mass of 125 GeV with the CMS experiment at the LHC*, Phys. Lett. B 716 (2012) 30, arXiv:1207.7235 [hep-ex].

[19] UA1 Collaboration, *Experimental observation of isolated large transverse energy electrons with associated missing energy at* $\sqrt{s}$ *= 540 GeV*, Phys. Lett. B 122 (1983) 103-116, CERN-EP-83-13; UA2 Collaboration, *Observation of single isolated electrons of high transverse momentum in events with missing transverse energy at the CERN pp collider*, Phys. Lett. B 122 (1983) 476-485, CERN-EP-83-25.

[20] UA1 Collaboration, *Experimental observation of lepton pairs of invariant mass around 95 GeV/*c^2 *at the CERN SPS collider*, Phys. Lett. B 126 (1983) 398-410, CERN-EP-83-073.

[21] The Physics Hypertextbook. *Beyond the Standard Model*.
Available from: http://physics.info/beyond/. [Accessed: 14/03/2014].

[22] Monica Young, 2013. *Beyond the Standard Model Or Not*.
Available from: http://www.skyandtelescope.com/news/home/Beyond-the-Standard-Model-mdash-Or-Not-186338072.html. [Accessed: 14/03/2014].

[23] Dark Matter. CERN. Available from: http://home.web.cern.ch/about/physics/dark-matter. [Accessed: 14/03/2014].

[24] Daniel Hayden, Raymond Brock, Christopher Willis,
Z Prime: A Story, arXiv:1308.5874, 2013.

[25] Fermilab, Z' *Gauge Bosons at the Tevatron*, hep-ph/0408098 FERMILAB-PUB-04-129-T.

[26] Thomas G. Rizzo, *Z Phenomenology and the LHC*, hep-ph/0610104 SLAC-PUB-12129.

[27] Paul Langacker, *The Physics of Heavy Z′ Gauge Bosons*, arXiv:0801.1345v3 [hep-ph], 2009.

[28] J. L. Hewett and T. G. Rizzo, *Low-energy phenomenology of superstring-inspired E6 models*, Phys. Rept.183 (1989) 193, doi:10.1016/0370-1573(89)90071-9.

[29] Lyndon Evans and Philip Bryant, *LHC Machine*, JINST 3 S08001 (2008).

[30] LHC Images. CERN. Available from: http://lhc-machine-outreach.web.cern.ch/lhc-machine-outreach/lhc_in_pictures.htm [Accessed: 17/03/2013].

[31] Prof. Dr. Ian C. Brock, *The ATLAS detector*, 2011. Available from: http://brock.physik.uni-bonn.de/atlas.php?lang=en [Accessed: 17/03/2013].

[32] HY.P.A.T.I.A, *Axes*, 2011. Available from: http://hypatia.iasa.gr/en/help.html. [Accessed: 17/03/2013].

[33] ATLAS Collaboration, *Reconstruction and Calibration of Missing Transverse Energy and Performance in Z and W events in ATLAS Proton-Proton Collisions at 7 TeV*, ATLAS-CONF-2011-080 (2011).

[34] ATLAS Experiment, *Events Explained*. Available from: http://www.atlas.ch/photos/full-detector.html [Accessed: 17/03/2013].

[35] R.K. Bock and A. Vasilescu, 1998. *The Particle Detector BriefBook*, Berlin Heidelberg: Springer.

[36] The ATLAS Experiment, *Inner Detector*.
Available from: http://atlas.ch/inner_detector.html [Accessed: 15/02/2014].

[37] P. Adragna, *The ATLAS Hadronic Tile Calorimeter: From Construction Toward Physics, IEEE Transactions on Nuclear Science*, vol. 53, issue 3, pp. 1275-1281 (2006).

[38] ATLAS Collaboration, *Readiness of the ATLAS Tile Calorimeter for LHC collisions*, arXiv:1007.5423, 2010.

[39] The Tile Calorimeter Group of the ATLAS Collaboration, *The Production and Qualification of Scintillator Tiles for the ATLAS Hadronic Calorimeter*, ATL-TILECAL-PUB-2007-010, 2008.

[40] ATLAS Collaboration, *Tile Calorimeter Technical Design Report*, CERN LHCC/96-42, 1996.

[41] ATLAS Collaboration, *Performance of the Reconstruction and Identification of Hadronic Tau Decays with ATLAS*, ATLAS-CONF-2011-152 (2011).

[42] Oleg Solovyanov, TileSr90Table.
Available from: https://twiki.cern.ch/twiki/bin/viewauth/Atlas/TileSr90Table [Accessed: 16/08/2013].

[43] ATLAS collaboration, *A search for high-mass ditau resonances decaying in the fully hadronic final state in pp collisions at $\sqrt{s}$ = 8 TeV with the ATLAS detector*, ATLAS-CONF-2013-066 (2013).

[44] D Emeliyanov and J Howard, *GPU-Based Tracking Algorithms for the ATLAS High-Level Trigger*, J. Phys.: Conf. Ser. 396 012018, 2012.

[45] T. Sjostrand, S. Mrenna, and P. Skands, *A Brief Introduction to Pythia 8.1*, Comput. Phys. Comm. 178 (2008) 852.

[46] ATLAS Collaboration, *Search for high-mass dilepton resonances in 20 fb-1 of pp collisions at $\sqrt{(s)}$ = 8 TeV*, ATL-COM-PHYS-2013-087, Jan, 2013.

[47] Philip Ilten, *Tau Decays in Pythia 8*, arXiv:1211.6730 [hep-ph].

[48] R. Gavin, Y. Li, F. Petriello, and S. Quackenbush, *FEWZ 2.0: A code for hadronic Z production at next-to-next-to-leading order*, Comput. Phys. Commun. 182 (2011) 23882403, arXiv:1011.3540 [hep-ph].

[49] GEANT4 Collaboration, S. Agostinelli et al., *GEANT4: A simulation toolkit, Nucl. Instr. and Meth*, A 506 (2003) 250.

[50] G. Duckeck et. al., *ATLAS computing: Technical Design Report, ATLAS TDR–017*, CERN-LHCC-2005-022.

[51] ATLAS Collaboration, *A search for high-mass resonances decaying to $\tau^+\tau^-$ in pp collisions at $\sqrt{s}$ = 7 TeV with the ATLAS detector*, Physics Letters B 719 (2013) no. 45, 242 260.

[52] T. Perez Cavalcanti, *Neural network based cluster reconstruction in the ATLAS silicon Pixel Detector*, JINST 8 C04003, 2013.